Fine-Tuning Melt Pools and Microstructures: Taming Cracks in Powder Bed Fusion—Laser Beam of a non-weldable Ni-base Superalloy

MTLA 34 (2024) 102059

Contents lists available at ScienceDirect

Materialia

journal homepage: www.elsevier.com/locate/mtla

Full Length Article

Fine-Tuning Melt Pools and Microstructures: Taming Cracks in Powder Bed Fusion—Laser Beam of a non-weldable Ni-base Superalloy

Ahmed Fardan [a,*], Andrea Fazi [b], Ru Lin Peng [c], Tatiana Mishurova [d], Mattias Thuvander [b], Giovanni Bruno [d,e], Håkan Brodin [a,f], Eduard Hryha [a]

[a] Department of Industrial and Materials Science, Chalmers University of Technology, 41296 Göteborg, Sweden
[b] Department of Physics, Chalmers University of Technology, 41296 Göteborg, Sweden
[c] Division of Engineering Materials, Department of Management and Engineering, Linköping University, 58183 Linköping, Sweden
[d] Bundesanstalt für Materialforschung und -Prüfung (BAM), Unter den Eichen 87, 12205 Berlin, Germany
[e] University of Potsdam, Institute of Physics and Astronomy, Kalr-Liebknecht-Str.24-25, 14476 Potsdam, Germany
[f] Siemens Energy AB, 612 83 Finspång, Sweden

ARTICLE INFO

Keywords:
Solidification cracking
CM247LC
Powder bed fusion – laser beam
Non-weldable superalloy
Ni-base superalloy

ABSTRACT

Powder Bed Fusion – Laser Beam (PBF-LB) of high γ' strengthened Ni-base superalloys, such as CM247LC, is of great interest for high temperature applications in gas turbines. However, PBF-LB of CM247LC is challenging due to the high cracking susceptibility during PBF-LB processing (solidification cracking) and heat treatment (strain age cracking, mostly caused by residual stresses). This study focuses on understanding the impact of process parameters on microstructure, residual stresses and solidification cracking. Laser power (*P*), speed (*v*) and hatch spacing (*h*) were varied while the layer thickness (*t*) was fixed. The melt pool size and shape were found to be key factors in minimizing solidification cracking. Narrower and shallower melt pools, achieved using a low line energy density ($LED = P/v \leq 0.1$ J/mm), gave low crack densities (0.7 mm/mm^2). A tight hatch spacing ($h =$ 0.03 mm) resulted in reduced lack of fusion porosity. Electron backscatter diffraction investigations revealed that parameters giving finer microstructure with ⟨100⟩ crystallographic texture had low crack densities provided they were processed with a low *LED*. Atom probe tomography elucidated early stages of spinodal decomposition in the as-built condition, where Cr and Al cluster separately. The extent of spinodal decomposition was found to be affected by the *LED* and the hatch spacing. Samples with low *LED* and small hatch spacing showed higher degrees of spinodal decomposition. X-ray diffraction residual stress investigations revealed that the residual stress is proportional to the volumetric energy density ($VED = P/(v.\ h.\ t)$). Although low residual stresses can be achieved by using low *VED*, there is a high risk of lack of fusion. Hence, other parameters such as modified scan strategy, build plate pre-heating and pulsed laser mode, must be further explored to minimize the residual stresses to reduce the strain age cracking susceptibility.

1. Introduction

Powder Bed fusion – Laser Beam (PBF-LB) is an additive manufacturing (AM) process, where a laser beam is used to melt powder particles layer-by-layer until the desired component is built. It is a complex process with parameters such as laser power, laser speed, hatch spacing, layer thickness and many more [1,2]. Despite PBF-LB being a complex process, it has garnered attention from a variety of industries due to its design freedom. One such industry is the gas turbine industry, where Ni-base superalloys are of high interest [3–5]. This interest is due to the possibility of having complex internal cooling channels for blades that bring a number of advantages, e.g. (i) increase the lifetime of the blade, (ii) require less cooling air or (iii) allow higher temperatures to be achieved, which can increase the engine efficiency [6]. Nonetheless, the adoption of PBF-LB to manufacture non-weldable Ni-base superalloys such as CM247LC is problematic due to its high cracking susceptibility. From the welding literature, it is known that there are different types of cracking such as solidification cracking, liquation cracking, ductility dip cracking and strain age cracking. Solidification and liquation cracking could be defined as 'hot cracking' that refers to the cracking mechanism

* Corresponding author.
E-mail address: fardan@chalmers.se (A. Fardan).

https://doi.org/10.1016/j.mtla.2024.102059
Received 22 December 2023; Accepted 9 March 2024
Available online 14 March 2024

occurring during solidification or in heat affected zones. On the other hand, ductility dip cracking and strain age cracking could be referred to as 'solid-state cracking' that occurs after solidification [7,8]. Both 'hot cracking' and 'solid-state cracking' are responsible for the increased cracking susceptibility of high γ' Ni-base superalloys such as CM247LC. However, there is a mixed opinion in literature as to which type of cracking leads to the high cracking susceptibility of CM247LC during the PBF-LB process. Certain studies [9–11] have shown only hot cracking to occur, whereas other studies [12,13] have claimed that solid-state cracking also occurs in CM247LC. This could be a matter of debate because solid-state cracking, such as strain age cracking, occurs when there is precipitation of γ' (along with the high residual stresses from the PBF-LB process). However, there is a lower risk of γ' precipitation during the PBF-LB process due to the high cooling rates. On the other hand, some studies [14,15] have convincingly shown that strain age cracking can occur after heat treatment of samples manufactured by PBF-LB. This is of high importance, since it is necessary to heat treat CM247LC to obtain the appropriate grain size and γ' precipitates.

Ni-base superalloys contain Ni as matrix element with ten or more alloying elements. The solidification interval is large due to the high number of alloying elements, which can make certain alloys such as CM247LC prone to solidification cracking. Solidification cracking has previously been observed in samples manufactured by PBF-LB of several alloys; IN939 [12,13], IN738LC [16–18], CM247LC [10–13,19,20] and IN713 [21,22]. These alloys have moderate to high γ' volume fraction (30 to 70 %) and can be classified as heritage alloys, i.e. they were developed for traditional manufacturing techniques such as casting. Certain studies [18] focusing on heritage alloys have attributed solidification cracking to grain boundary segregation of minor alloying elements such as B, Zr and Hf. Removing these elements can significantly reduce the occurrence of solidification cracking during the PBF-LB process, possibly thanks to a reduced solidification interval [10]. However, these elements are crucial for properties such as creep, which is important for high temperature applications [23–26]. Apart from the above-mentioned standard heritage alloys, there have also been attempts to design and study novel Ni-base alloys [8,12,21,27–29]. Such novel alloys would require rigorous testing before they could replace the existing standard heritage alloys that were manufactured through conventional manufacturing techniques. Nearly crack-free CM247LC has been manufactured by systematically modifying the laser parameters (power, speed and hatch) [11,30]. But crack-free samples by Gerstgrasser et al. [31] was achieved using defocused laser which possibly cannot be done in all PBF-LB machines. It is to be noted from the literature on CM247LC manufactured by PBF-LB that less emphasis has been placed on understanding the impact of process parameters on microstructure, grain morphology/texture and cracking.

The approach taken in this study involving the CM247LC alloy was to understand the impact of the PBF-LB process parameters on microstructure, grain morphology/texture and cracking. There have been some studies on the PBF-LB processability of CM247LC [11,15,20,30] but none of them have particularly focused on linking process parameters, melt pool, cracking, residual stress and microstructure. These aspects are considered hereafter. The study aimed at correlating the quantified defects (crack density and porosity) with melt pool measurements for samples printed with varying parameters (power, speed, and hatch). Selected samples were investigated for microstructure, grain morphology, residual stresses, and element clustering. One of the main findings is that the cracking is minimal for specimens processed with a low line energy density (*LED* = Power/Speed). Another crucial finding is that the as-built CM247LC exhibits signs of early stages of spinodal decomposition, as Cr and Al and other elements partition. Also, the extent of the spinodal decomposition is found to be affected by the process parameters, possibly because of the complex thermal history and extensive remelting for the selected PBF-LB parameters.

2. Methodology

2.1. Material

Gas atomized CM247LC powder with a particle size range of 15 to 45 μm was provided by Höganäs AB (Höganäs, Sweden) as feedstock material. The powder used for printing was in the virgin state. The chemical composition of the CM247LC powder and PBF-LB part is provided in Table 1. C and O were measured using combustion and fusion analysis, respectively. The remaining elements were measured using ICP-OES analysis.

2.2. PBF-LB process

The parts were printed using an EOS M290 (Electro Optical Systems GmbH, Krailling, Germany) machine. This machine has a Yb-fiber laser with a maximum power of 400 W and a laser spot size of about 80 μm. A DOE (design of experiment) was performed on cubes of 10 × 10 × 10 mm^3 with varying laser power, laser speed, and hatch spacing, while the layer thickness was fixed at 30 μm. The DOE consisted of a custom DOE to scan across a wide processing window. The set-up of the DOE is shown in Table 2. The DOE was performed for only the infill parameters and no contour parameters were performed for any samples throughout this study. In the DOE, volumetric energy densities (Eq. (1)) within the range of 50 to 130 J/mm^3 were considered for printing. For all the printing parameters, a stripe scan strategy with a stripe width of 5 mm and a stripe overlap of 0.12 mm were used with a scan rotation of 67°. Build plate preheating of 80 °C was used.

$$VED = \frac{P}{v.h.t} \tag{1}$$

where P is laser power, v is laser speed, h is hatch spacing and t is layer thickness.

2.3. Normalized processing diagram

The normalized processing diagram was employed to enable direct comparison of this study with other studies in literature [19,20,32]. The normalization for the PBF process was developed by Thomas et al. [33] and was based on an earlier work by Ion et al. [34] for laser materials processing. Numerous studies have used parameters such as energy density (line, surface or volumetric) to compare process parameters. Such parameters can differ based on AM machine manufacturer due to differences in laser beam radius and preheating temperature. The latter are not considered within the standard energy density (using power, speed, hatch, and layer thickness). Using a normalized processing diagram to plot parameters aids in identifying different processing regimes such as lack of fusion, keyhole, and solidification cracking window.

The normalized processing diagram uses dimensionless quantities. A brief derivation of the equations used to normalize is shown here, but the reader is referred to Thomas et al. [33] for a detailed explanation. The hatch spacing h is normalized with the beam radius r_B to yield a dimensionless hatch spacing:

$$h^* = h/r_B \tag{2}$$

The normalized heat input per unit volume is:

$$E^* = P^*/v^* t^* \tag{3}$$

In Eq. (3), P^* refers to the dimensionless beam power, v^* refers to the dimensionless beam velocity and t^* is the dimensionless layer thickness. The respective equation for these dimensionless quantities can be found in Thomas et al. [30], which when substituted to Eq. (3) yield the dimensionless volumetric energy density:

$$E^* = P^*/v^* t^* = [AP/(2vtr_B)]\left[1/0.67\rho C_p(T_m - T_0)\right] \tag{4}$$

Table 1
Chemical composition of the CM247LC powder and PBF-LB part (at.% and wt.%) used in this study.

		Cr	Co	Mo	C	W	Hf	Ta	Ti	Al	Zr	B	Si	O	Ni
Powder	at.%	9.20	9.43	0.31	0.30	3.15	0.44	1.06	1.00	12.40	0.006	0.06	0.17	0.04	Bal.
	wt.%	8	9.3	0.5	0.06	9.7	1.3	3.2	0.8	5.6	0.009	0.01	0.08	0.01	Bal.
PBF-LB part	at.%	9.29	9.21	0.34	0.30	3.08	0.45	1.02	1.00	12.16	0.01	0.10	0.23	0.02	Bal.
	wt.%	8.1	9.1	0.54	0.06	9.5	1.34	3.1	0.8	5.5	0.011	0.019	0.11	0.005	Bal.

Table 2
DOE parameters used in this study of CM247LC along with some parameters from the literature.

	AM machine	Scan Strategy	Bed Temperature	Power	Speed	Hatch	Layer thickness	Beam radius
			T_0	P	v	h	t	r_B
			K	W	m/s	m (10^{-6})	m (10^{-6})	m (10^{-6})
This study	EOS M290	Stripe	353	100 - 300	1 - 3	30 – 90	30	50
Carter et al. [19,32]	Concept Laser M2	Chessboard	298	100 - 200	0.4 - 2	30 – 80	20	75
Adegoke et al. [20]	EOS M290	Stripe	353	170 - 220	2.8 – 3.2	20– 40	20	50

where A is the surface absorptivity or coupling coefficient, r_B is the beam radius, ρ is the density, C_p is the specific heat capacity, T_m is the melting temperature and T_0 is the initial temperature (powder bed temperature). The normalized processing diagram for CM247LC was plotted using the parameters shown in Table 2 along thermophysical parameters obtained from Mukai et al. [35] and Avala et al. [36] summarized in Table A1 in Appendix A.

2.4. Microstructural characterization

The cross-section along the build direction was used for microstructural investigations. The sample was mounted in conductive bakelite resin and ground using SiC papers (#320, #500, #800 and #1200) using a Struers Tegrapol. This was followed by polishing using a diamond suspension of 3 μm on a taffeta woven wool surface (MD-Mol by Struers) and finally 1 μm polishing was employed. Light Optical Microscopy (LOM) measurements were made using Zeiss Axiovision 7. The defect analysis consisted of acquiring images at a magnification of 100X as shown in [19] and then using ImageJ software for defect quantification. The crack density analysis was performed by manually measuring the total crack length (in mm) and dividing it by the analyzed area (in mm^2) to yield crack density (in mm/mm^2). The relative density was acquired by measuring the porosity by applying a threshold on binarized images that was then subtracted from 100 %. Before high resolution Scanning Electron Microscopy (SEM) analysis using Leo Gemini 1550 SEM, the surface underwent a final step of polishing using 0.05 μm colloidal silica (Struers OPS) to remove any deformation caused by previous grinding/polishing. Electron Backscatter Diffraction (EBSD) analysis was performed using Leo Gemini 1550 SEM equipped with Nordlys II detector (Oxford Instruments, Abingdon, Oxfordshire, England). EBSD analysis was performed using an accelerating voltage of 20 kV and an aperture size of 120 μm. A step size of 2 μm was used for overall texture analysis at a magnification of 200X. The EBSD data were plotted using the open source MTEX toolbar (version 5.9.0) in MATLAB. To reveal the solidification structure and microstructural features, the samples were swab etched using Kalling's 2 (Water Kallings, 5 g $CuCl_2$ + 100 ml 37 % HCl + 100 ml ethanol). The melt pool width and depth measurements were performed using ImageJ on etched LOM micrographs of the topmost layer. Three measurements for each melt pool (width and depth) were carried out, and the average value was calculated (and reported throughout the remainder of the study).

2.5. Atom probe tomography (APT) measurements

The atom probe measurements were performed using a local electrode atom probe LEAP 6000 XR from CAMECA (Madison, Wisconsin, US). The instrument was used in laser pulse mode at 50 K specimen temperature, 0.5–1.0% evaporation rate, and 30–35 pJ laser energy. Auto pulse frequency control was implemented and set to guarantee a minimum mass spectrum range of 180 Da. APT specimens were fabricated by electropolishing of rods (section: $0.3 \times 0.3\ mm^2$, length: 10 mm extracted from a 10 mm cube) in a layer of 10 % perchloric acid dissolved in methanol on top of an inert fluorinated solution (Galden® PFPE). Once a neck was formed, a second electropolishing step was performed in 2 % perchloric acid dissolved in 2-butoxyethanol to separate the two ends of the neck and form sharp needles. Any remaining surface oxide was removed by voltage pulsing (5 pulses, 5 milliseconds long) in 2 % perchloric acid in butoxyethanol. The voltage was 20 V in all steps.

2.6. Residual stress measurements

Residual stresses in the selected PBF-LB samples were evaluated using the X-ray diffraction (XRD) method on cuboids ($10 \times 10 \times 15\ mm^3$). Like any other diffraction-based methods for residual stress measurements, the crystal lattice is used as an internal strain gauge. Changes in the interplanar spacing due to residual stresses are measured and the corresponding residual stresses are then determined using the appropriate diffraction elastic constants.

A Seifert X-ray diffractometer equipped with a Cr X-ray tube and a linear position sensitive detector was used in the current work. In-plane residual stress components parallel as well as perpendicular to the building direction were measured on a surface facing the gas inlet and at a position of 5 mm from the top surface. A collimator of 2 mm in diameter was used on the incident beam side. Diffraction peaks of $\gamma-220$ lattice planes were measured in 21 sample directions evenly spread between $\sin^2(\psi=\pm 60^\circ)$ and $\sin^2(\psi=0^\circ)$. A pseudo-Voigt function was fitted to the obtained diffraction peaks to determine the interplanar spacings, from which residual stresses were calculated via the widely used "$\sin^2\psi$" technique [37] with the X-ray elastic constant $1/s_2 = 4.905\ TPa^{-1}$ [38]. With the Cr-K_α radiation, the diffraction peaks appeared at about 129.2° in 2θ.

Surface residual stresses were measured on the as-built samples without any surface preparation. To obtain residual stress values in subsurface layers, some material was removed layer-wise by electrolytic polishing. Residual stress relaxation due to the layer removal procedure was not considered because of the (small) size of the etched area.

2.7. X-ray computed tomography (XCT) measurements

X-ray Computed Tomography (XCT) was used to evaluate the volume and spatial distribution of cracks in 3D. The samples printed for XCT

were cylinders of 3 mm diameter and 10 mm length to facilitate the use of smaller voxel size. The XCT measurements were performed using a v|tome|x L 300 CT scanner from General Electric. With an acquisition time of 3 s for each projection, 2500 projections were acquired during each scan. A tube voltage of 160 kV, a current of 60 μA with a voxel size of 3 μm were used. The segmentation of cracks was performed in the Dragonfly software (Object Research Systems, Inc, Montreal, Quebec, Canada) [39] using a deep learning algorithm. To provide the training data for the neural network different classes were annotated as the corresponding phases: material, cracks, pores, and background. They were manually labeled on a few 2D cross-sections for each data set and then a U-Net model was trained on the segmented slices. The training of the U-Net model was divided in so-called epochs with a loss function, representing the progress of the training after each epoch. With the progress, the coefficient of the loss function decreases as a function of the epoch number until it stabilizes, and no more changes were visible. After this point, the model was considered trained and was applied to all slices in the dataset. 3D data visualization was performed by using the AvizoFire 9.4 software.

3. Results

3.1. PBF-LB processing and microstructure

The PBF-LB processing of CM247LC was challenging due to its high susceptibility to cracking during printing. This can be observed from the examination of the as-polished micrographs shown in Fig. 1 and Table 3, which shows the crack density values. In Fig. 1, it is observed that less cracking is obtained for samples with *LED* of 0.1 J/mm regardless of the hatch spacing (Fig. 1**(a)–(c)**). However, it is seen that there is a risk of insufficient melting leading to lack of fusion at a standard hatch spacing of 0.09 mm at a *LED* of 0.1 J/mm. In micrographs Fig. 1**(c), (e), (f)**, it is seen that there is an increase in cracking as *LED* increases from 0.1 to 0.3 J/mm for a fixed hatch spacing of 0.09 mm. So, the key to defect-free processing of CM247LC by PBF-LB is processing at low *LED* to minimize cracking and at the same time high enough *VED* to assure absence of lack-of fusion defects. Hence, the results show that PBF-LB processing with low *LED* (~0.1 J/mm) allows to minimize cracking and utilization of a low hatch spacing (~0.03 to 0.06 mm) allows to minimize lack of fusion. This can be explained from the simple volumetric energy density (Eq. (1)). So, when we have a low line energy density ($LED = P/v$), we need to have lower hatch spacing to have sufficiently high *VED* to have sufficient melting to avoid lack of fusion.

Table 3
Crack density values (in mm/mm2) for samples (shown in Fig. 1) with different *LED* and hatch spacing. '-' refers to samples that were not manufactured.

Hatch spacing (mm) *LED* (J/mm)	0.03	0.06	0.09
0.1	2.19	1.74	1.28
0.2	–	2.16	3.23
0.3	–	–	4.91

The as-built microstructure of CM247LC for a selected process parameter is shown in Fig. 2. This sample was processed with $P = 200$ W, $v = 3000$ mm/s and $h = 0.03$ mm. Such parameters correspond to a *VED* $= 74$ J/mm^3 and *LED* $= 0.07$ J/mm. An overview micrograph containing a crack and a lack of fusion void is shown in Fig. 2**(a)**. The inserts (b) and (c) highlight the regions shown in Fig. 2**(b)** and Fig. 2**(c)**. The crack surface is rough i.e. presence of dendrites indicating that the cracks

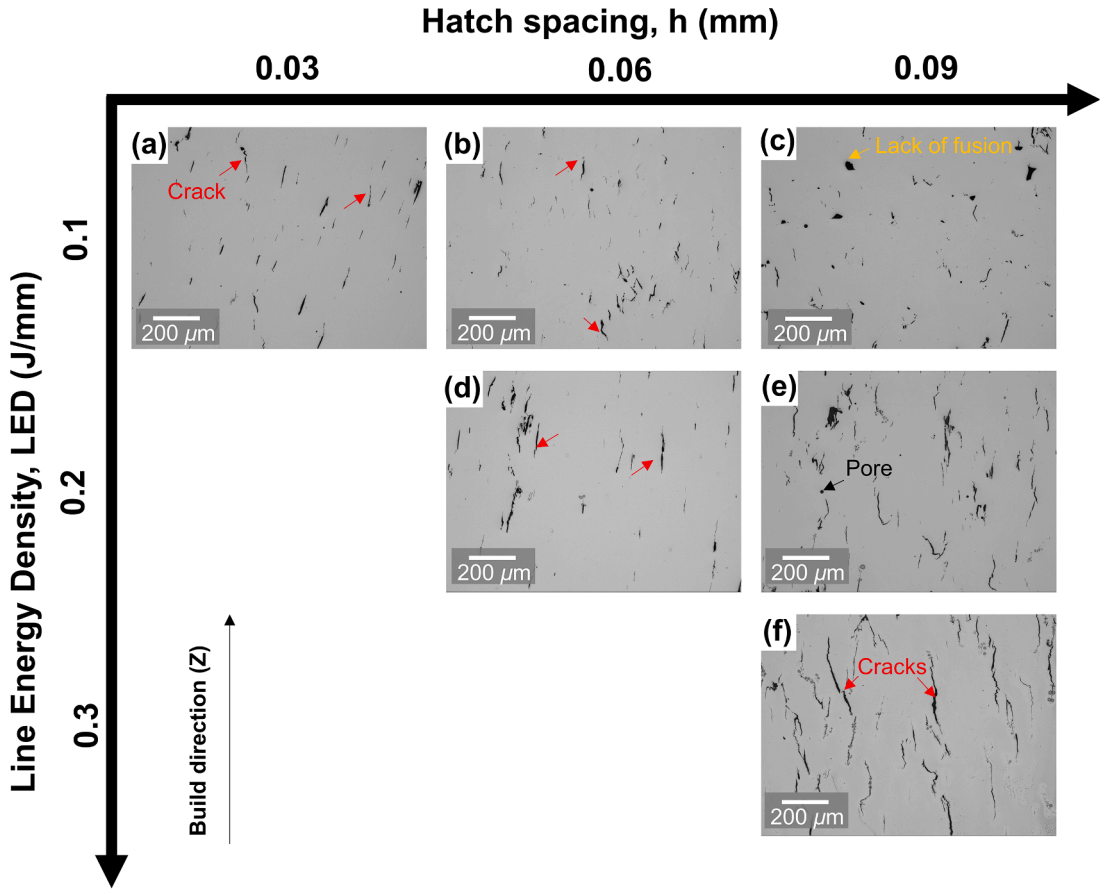

Fig. 1. Selected micrographs showing the presence of cracks, pores, and lack of fusion for different *LED* and hatch spacing. Red arrows in (a), (b), (d) and (f) indicate cracks. Lack of fusion is indicated in (c). A pore is indicated in (e). The empty regions indicate samples that were not feasible to manufacture.

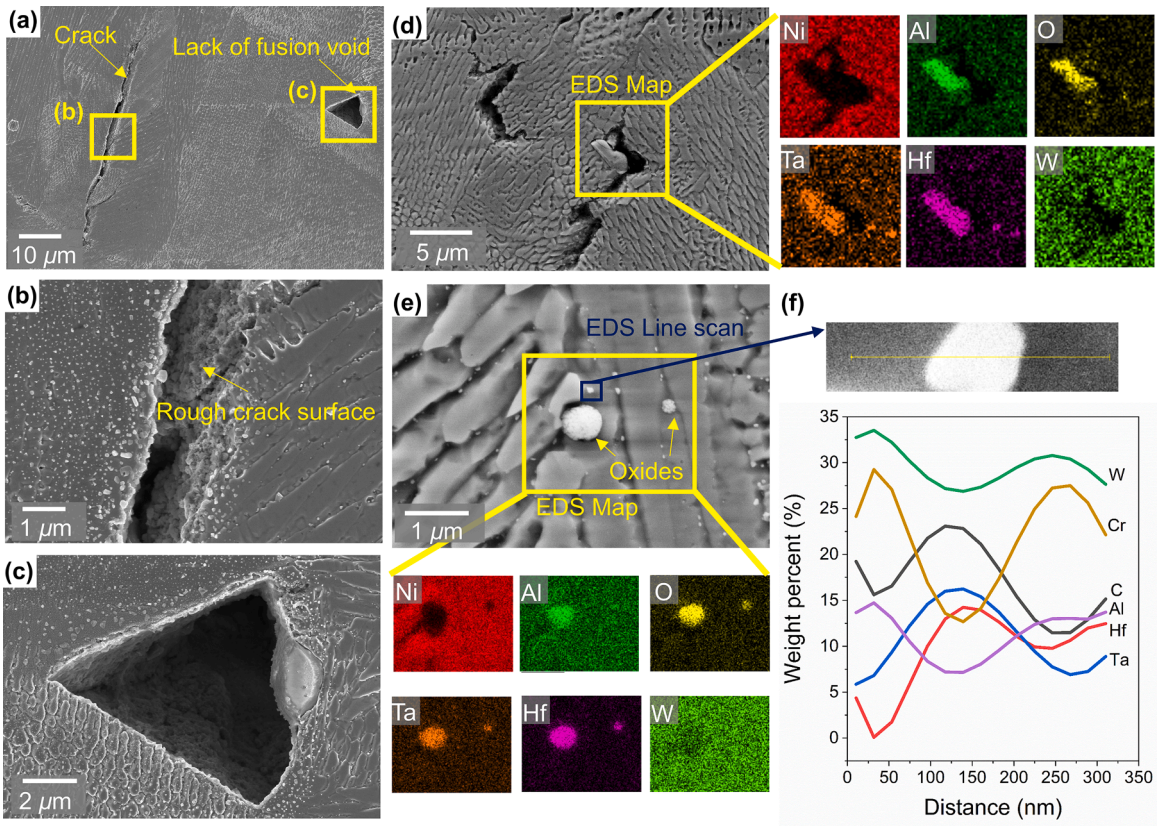

Fig. 2. **(a)** SEM micrograph showing a crack and a lack of fusion void, **(b)** and **(c)** are magnified images of the locations indicated in (a), **(d)** SEM micrograph showing cracks and an oxide inclusion with EDS, **(e)** SEM micrograph showing the presence of oxide inclusions with EDS and carbides, **(f)** EDS line scan of the carbide particle marked in Figure 2(e).

observed in CM247LC are most probably solidification cracks (Fig. 2 **(b)**). However, there is a possibility of solid-state cracking (strain age cracking) occurring in CM247LC due to the high γ' content, but this will be further described and discussed in Section 3.5 and in Section 4. Fig. 2 **(c)** shows a lack of fusion void with an irregular shape. The presence of oxides rich in Hf, Ta and Al were also found in a crack vicinity (Fig. 2**(d)**) and in the bulk (Fig. 2**(e)**). Also, fine bright particles can be noticed in Fig. 2**(b), (c)** and **(e)**. An EDS line scan was performed on one such bright particle marked in Fig 2**(e)**. The scan shows that the particles are MC-type carbides rich in Hf and Ta.

The processing parameters in this study were compared with Carter et al. [19] and Adegoke et al. [20] on the normalized processing diagram

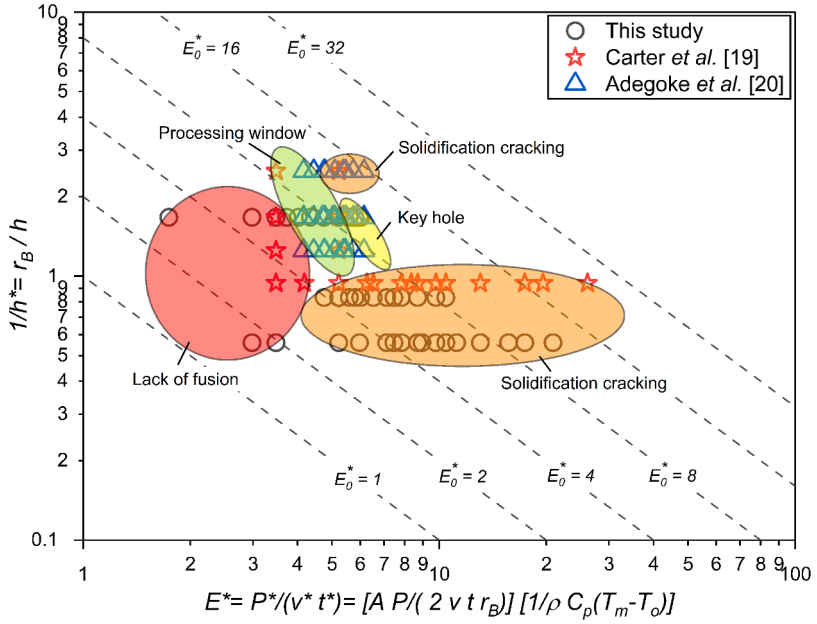

Fig. 3. Normalized processing diagram of CM247LC with data from this study and with parameter data extracted from Carter et al. [19] and Adegoke et al. [20].

in Fig. 3. The y-axis is the inverse of the normalized hatch spacing h^* (which means that a high $1/h^*$ value corresponds to a small hatch spacing) calculated using Eq. (2) and the x-axis is the normalized heat input per unit volume (E^*) calculated using Eq. (4). The normalized diagram allows a direct comparison between the results from this study and the literature. The isopleths E_0^* represent the normalized equivalent energy where higher values of E_0^* represents a higher heat input and lower E_0^* might lead to insufficient melting and lack of fusion voids. The different processing regimes were identified from the porosity and crack density calculations along with input from the literature. It is to be noted that samples cannot be printed crack-free. Therefore, the processing window refers to samples that can be obtained with low crack density that can be considered nearly crack-free. From Fig. 3, it is seen that for $E_0^* \leq 3$ the parameters yielded more lack of fusion, as indicated by a red circle. The parameter space $3 \leq E_0^* \leq 32$ and $1/h^* \leq 1$ resulted in large amounts of solidification cracking. The processing window is quite narrow and is found to be at $6 \leq E_0^* \leq 10$ and $1/h^* \geq 1$. This shows that CM247LC is sensitive to cracking and that hatch spacing $h \leq r_B$ should be employed. Also, a second region of solidification cracking and keyhole formation was identified at approximately $E_0^* \geq 8$ and $1/h^* \geq 1$. This is probably due to excessive re-melting occurring at low hatch spacing and high heat input. Although the normalized diagram gives a good understanding of the different processing regimes, it is crucial to examine the melt pool dimensions and overlap which can elucidate more about the relation between processing parameters and solidification cracking.

The entire parameter set is used to show the relationship between *LED*, melt pool dimensions/overlap and crack density, see Fig. 4. The horizontal and vertical overlap (in %) are calculated by Eq. (5) and (6), respectively.

$$Horizontal\ overlap\ (\%) = \left(1 - \frac{hatch\ spacing}{Melt\ pool\ width}\right) \times 100 \tag{5}$$

$$Vertical\ overlap\ (\%) = \left(1 - \frac{layer\ thickness}{Melt\ pool\ depth}\right) \times 100 \tag{6}$$

It is observed that the melt pool depth has a linear relationship with *LED* (Fig. 4**(a)**). The R^2 coefficient for the linear fit was found to be 0.83. The combination of low h and *LED* leads to shallow melt pools, as observed from Fig. 4**(a)**. Such melt pools are found to have low crack density (as indicated by the color bar). The linear fit of the melt pool width vs. *LED* yielded a poor correlation, with an R^2 coefficient of 0.61 (Fig. 4**(b)**). However, a similar trend to melt pool depth is also observed with melt pool width where low h and *LED* is found to give low crack density. The relation between horizontal and vertical overlap of the melt pool with crack density is shown in Fig. 4**(c)**. It is seen that a hatch of 0.03 mm gives a new processing regime with large horizontal overlap and small vertical overlap and low crack density. To sum up, shallow melt pools with strong overlap are the key to processing CM247LC. This regime is achieved through a low *LED* and a small hatch spacing.

3.2. Grain morphology and texture

EBSD maps were acquired for samples with different *LED* and hatch spacing (Fig. 5). The chosen samples and the figure layout are the same as for the optical micrographs shown in Fig. 1 with respect to hatch spacing and *LED*. The EBSD maps are plotted with inverse pole figure representation along the build direction (Z). The (100) pole figures and the intensity for the respective EBSD maps are also plotted. In the pole figure, the build direction is in the center of the pole figure. In addition

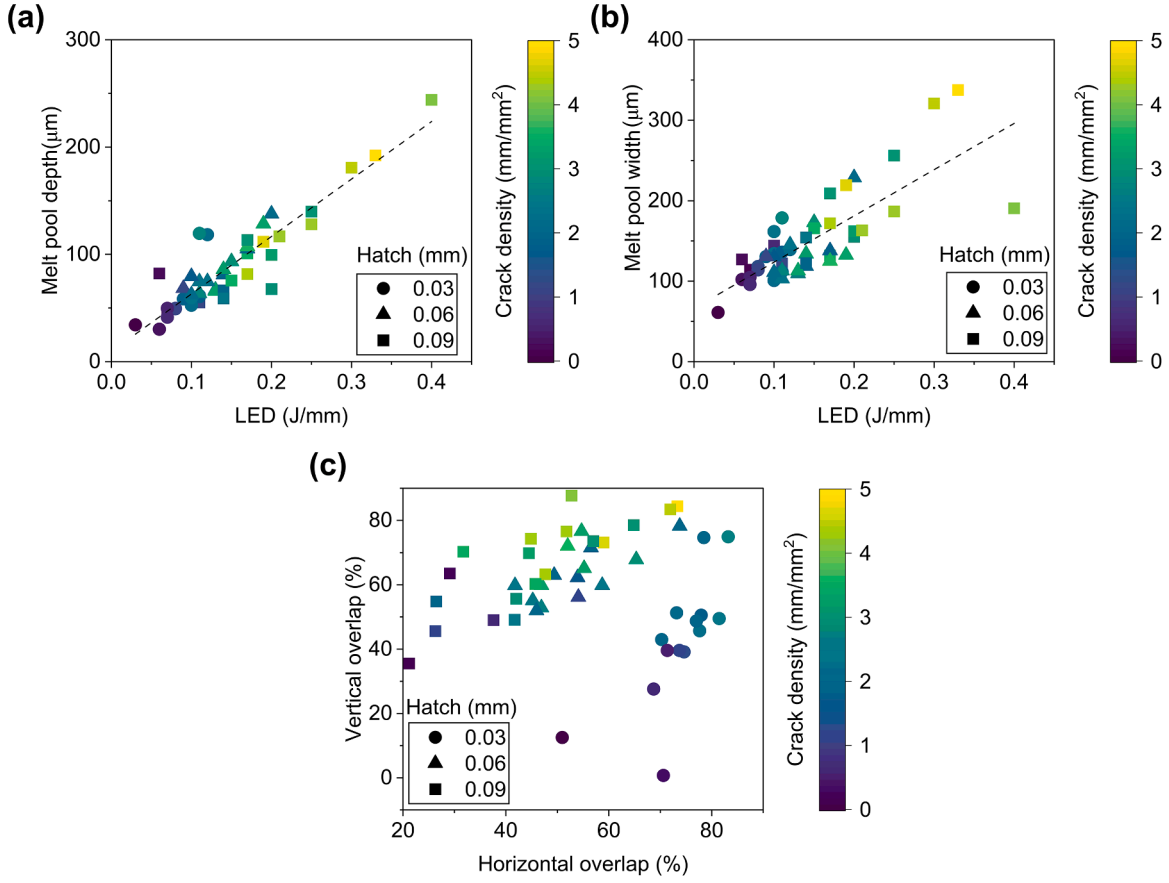

Fig. 4. Scatter plot of crack density as a function of **(a)** Melt pool depth and *LED* (line energy density), **(b)** Melt pool width and *LED*, **(c)** vertical and horizontal overlap of melt pool.

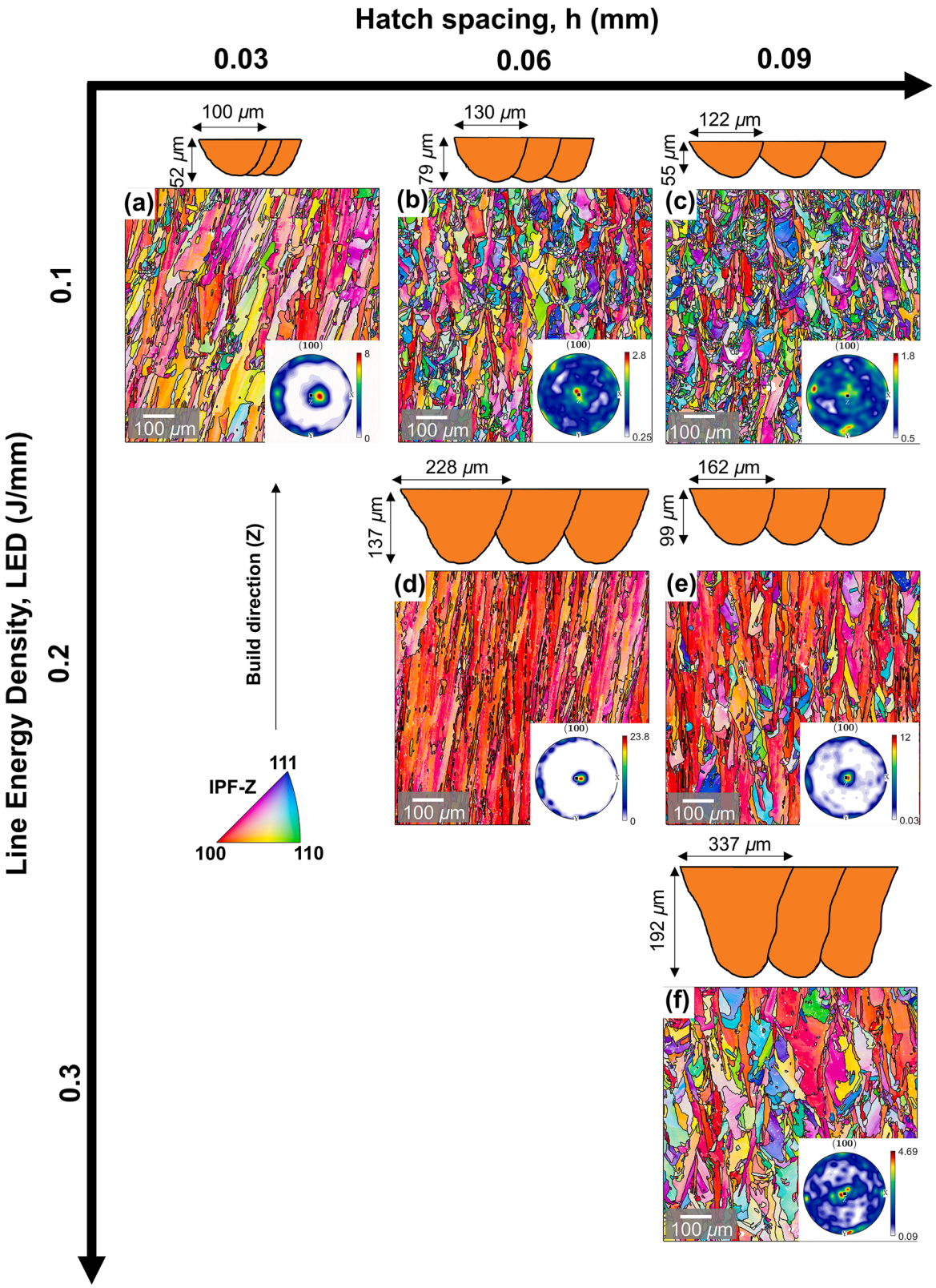

Fig. 5. EBSD orientation in inverse pole figure representation and the corresponding (100) pole figure for different parameters along with schematics of the melt pool geometries.

to this, the schematic of the melt pool and the melt pool dimensions obtained from Fig. C1 in Appendix C are also added for the respective EBSD maps.

The sample with the lowest *LED* (0.1 J/mm) and hatch spacing (0.03 mm) is seen to have the smallest and the shallowest melt pools with strong horizontal overlap (Fig. 5**(a)**). This parameter condition is also found to give columnar grains with the strongest ⟨100⟩ texture (texture intensity of 8), but as the hatch spacing increases to 0.06 mm and 0.09

mm it is found that there is a weaker texture and a more refined microstructure with smaller grains. For *LED* of 0.2 J/mm and hatch spacing of 0.03 mm, the *VED* was approximately 222 J/mm^3. Such a high energy input leads to swelling in the part leading to recoater crashes and hence deliberately was not built for characterization. However, a specimen with hatch spacing of 0.06 mm could be built and showed larger melt pool width and depth (Fig. 5**(d)**) than sample with *LED* of 0.1 J/mm (Fig. 5**(b)**). The large melt pool dimension led to columnar grains and a strong ⟨100⟩ texture with a pole intensity of 24. By increasing the hatch distance to $h = 0.09$ mm, a weaker texture with a pole intensity of 12 was obtained. Finally, with $LED = 0.3$ J/mm and $h = 0.09$ mm, there is presence of larger grains with weaker texture than the specimens with $LED = 0.2$ J/mm.

3.3. Residual stress

Four samples processed with different parameters (energy densities (*LED* and *VED,* see Table 4) were chosen for residual stress analysis. The optical micrographs (Fig. 6) and the area fraction from image analysis in Table 4 show that they have different defect quantities, as different *LEDs* led to different melt pool geometries. The melt pool sketches and dimensions were obtained from obtained from Fig. C2 in Appendix C. These four samples for residual stress analysis and for X-ray computed tomography in Section 3.4 were chosen as exemplarily representing the effect of different *VED* on residual stress. Additionally, these samples did not have high defect fraction. Such feature makes them suitable candidates for HIP. It is seen from Fig. 6 that P2 has shallower and narrower melt pools than P1; this led to a higher crack density in P1 (2.90 mm/mm^2). However, it is seen that P3 (*LED* of 0.10 J/mm) has higher crack density than P2 (*LED* of 0.07 J/mm), as shown in Table 4, although the two samples have similar melt pool geometries (Fig. 6). This shows that even though it is beneficial to have shallow and narrow melt pools, it is also crucial to have sufficiently low *LED*.

The residual stress depth profiles that were measured for the four samples mentioned above are shown in Fig. 6. The profiles were obtained until a depth of ~200 μm. This is because low tensile residual stresses are usually detected closer to the surface due to surface roughness (attached powder particles) and finer grains closer to the surface [40]. It can also be clearly observed from Fig. 6 that maximum residual stress values are obtained at a distance of 100 μm from the surface. This justifies the reason for stress profiling until a depth of 200 μm and is also sufficient for comparison of the samples. Furthermore, only the residual stress component along the build direction is reported as the stress values are much higher than in the transverse direction.

In general, the residual stress increases with increasing distance from the surface regardless of the parameters. It can also be seen that P1 and P2, processed with the same *VED* (74 J/mm^3), have similar residual stress values at distances greater than 50 μm. P3, processed with a *VED* of 111 J/mm^3 had similar residual stress as P1 and P2 up to a distance of 100 μm. At greater distance from the surface, the residual stress sharply increases, reaching approximately 1200 MPa. P4, processed with a *VED* of 53 J/mm^3, had relatively low residual stress values. The residual stress for P4 increases with the increasing distance from the surface and reaches a plateau of about 800 MPa at a depth of approximately 125 μm. These values are consistent with the literature [41].

In general, the maximum residual stress values are dependent on the *VED*. Higher *VED* leads to higher residual stress values while lower *VED* leads to lower residual stress values. Samples with the same *VED* but different laser process parameters had similar residual stress values. It can also be observed that the residual stress values reported here for CM247LC (900 to 1200 MPa) is greater than reported stress values of IN718 manufactured by PBF-LB [40]. Due to the differences in the alloy and processing condition, one must be wary when comparing different alloy systems. Further clarifications of the high residual stresses for CM247LC can be found in Section 4.3.

3.4. X-ray computed tomography (XCT)

The crack distribution obtained by XCT for specimens P1, P2, P3 and P4 are presented in Fig. 7 along with the melt pool geometries and crack volume percentage. All the samples presented an interconnected network of cracks in 3D but with different crack densities. Although the 2D and 3D crack density estimation methods are somewhat different, the values of area crack density (see Table 4) qualitatively correspond to the volumetric values.

From Table 4 and Fig. 7, we can see that the *VED* solely does not explain the cracking behavior. However, there is a clear indication that *LED* and the normalized energy input E^* can be correlated with the crack density/volume. This is because it is possible to have different parameters but the same *VED* (for example, P1 and P4 in Table 4) but different cracking behaviors. This is because the cracking is dependent on melt pool geometry which in turn is dictated by *LED* and/or E^* (*LED* and E^* are proportional). This behavior is observed clearly in Fig. 7 where low *LED* and E^* (parameter set P3) leads to low crack density/volume. And the severity of cracking increases at higher *LED* and E^*. In such a case, cracks become deep and have plate-like morphology in Fig. 7**(g)**. On the other hand, we observe that in Fig. 7**(f)**, we have shallower cracks for P2 (*LED* of 0.07 and E^* of 1.74). Another observation from the XCT data (Fig. 7) is that cracking does not extend to the surface in P2 unlike P1, P3 and P4. Since cracks open to the surface cannot be healed during HIP, it becomes crucial to choose low *LED* and E^*.

3.5. Atom probe tomography (APT)

APT was performed to reveal the impact of processing parameters on possibility and extent of γ' precipitation in the as-built state and hence risk of strain age cracking. Three samples with similar *VED* but increasing line energy density and hatch spacing were selected for APT. The chosen samples had increasing crack density which can also be observed in Fig. 1**(a), (d), (f)**. Fig. 8 shows atom maps and the corresponding radial distribution function (RDF) plots. It also contains the schematic of the melt pool geometries. The RDFs were calculated in a box of $30 \times 30 \times 30$ nm^3 with Cr atoms as centers up to a radius of 20 nm and a step size of 0.2 nm. RDFs for the entire run were also calculated and showed the same trends and features. RDF is a powerful statistical tool that can show early stages of phase separation or clustering, and spinodal decomposition, which is suspected to be occurring in the as-built material of CM247LC [42,43].

From the APT results (in Fig. 8), no γ' precipitation was detected in any of the samples. However, spinodal decomposition was observed in

Table 4
Process parameters used for residual stress and X-ray computed tomography measurements.

	Power	*Speed*	*Hatch*	*LED*	*VED*	*E**	Area fraction from Image analysis		Volume fraction from XCT	
	P	*v*	*h*				Crack density	Porosity	Crack	Porosity
	W	*mm/s*	*mm*	*J/mm*	*J/mm^3*	–	*mm/mm^2*	*%*	*%*	*%*
P1	100	500	0.09	0.20	74	5.22	2.90	0.38	6.03	–
P2	200	3000	0.03	0.07	74	1.74	0.74	0.28	1.53	0.01
P3	300	3000	0.03	0.10	111	2.61	2.25	0.13	4.42	–
P4	200	1750	0.09	0.11	53	2.98	1.28	0.92	2.96	0.31

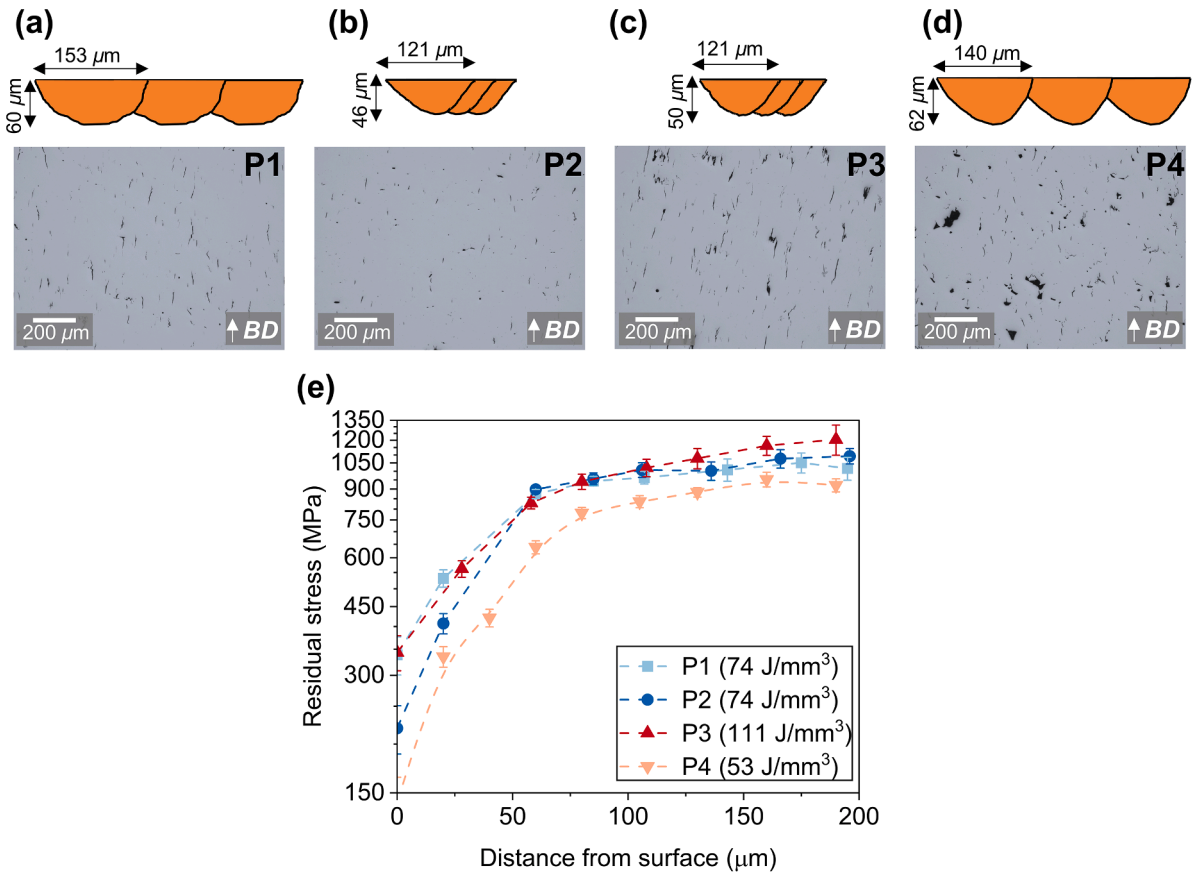

Fig. 6. Melt pool geometry and optical micrographs of samples built with parameters **(a)** P1 (74 J/mm^3): $P = 100$ W, $v = 500$ mm/s, $h = 0.09$ mm, **(b)** P2 (74 J/mm^3): $P = 200$ W, $v = 3000$ mm/s, $h = 0.03$ mm, **(c)** P3 (111 J/mm^3): $P = 300$ W, $v = 3000$ mm/s, $h = 0.03$ mm, **(d)** P4 (53 J/mm^3): $P = 200$ W, $v = 1750$ mm/s, $h = 0.09$ mm, **(e)** Depth profile of residual stress (along the BD), obtained using XRD and electrolytic polishing, for process parameters P1, P2, P3 and P4. BD = building direction.

as-built CM247LC. Two types of regions, namely Cr-rich regions (indicated by iso-surfaces of 9.5 at.% Cr displayed in magenta) and Al-rich regions (indicated by Al points plotted in cyan) which are enriched by Cr and Al atoms, respectively (shown in Fig. 8), were observed. The shape of the two types of regions (Cr and Al-rich) are also affected by the processing conditions. The anisotropic elongated features for the sample processed with *LED* = 0.1 J/mm (Fig. 8**(a)**) and Fig. B1 (a), (d), (g) (in Appendix B) along the build direction were observed. The regions are more isotropic for samples processed with *LED* of 0.2 J/mm (Fig. 8**(b)**) and *LED* of 0.3 J/mm (Fig. 8**(c)**). Visually the Cr and Al-rich regions appear to be relatively finer in Fig. 8**(b)** and Fig. B1 (b), (e), (h) for *LED* of 0.2 J/mm than Fig. 8**(c)** and Fig. B1 (c), (f), (i) for *LED* of 0.3 J/mm. It is clear from the RDFs (Fig. 8) that all the samples undergo spinodal decomposition, however, the extent of decomposition is found to be influenced by the processing parameters. It was noticed that samples processed with *LED* of 0.2 J/mm and 0.3 J/mm are less decomposed than the sample processed with *LED* of 0.1 J/mm. The maximum Cr concentration at the center of the Cr-rich regions displayed by the RDF of these two samples is lower than the maximum Cr concentration calculated for the *LED* 0.1 J/mm sample. Moving to larger distances, the Cr concentration falls below the bulk average, then it increases again and reaches a local maximum. These local maxima can be used to estimate the wavelength of the spinodal decomposition: higher values correspond to higher degrees of decomposition [42]. It can be observed that the first maximum occurs at different distances in different samples, indicating that the spinodal decomposition wavelength is affected by the processing parameters. The maximum for the sample with *LED* of 0.1 J/mm occurs at a distance of 12.8 nm while for *LED* of 0.2 J/mm and 0.3 J/mm the maximum occurs at shorter distances of 8.4 nm and 9.4 nm, respectively. This means that there is a higher probability of finding a Cr-rich region (from Cr-atoms as centre) at shorter distances for samples processed with high *LED* (0.2 and 0.3 J/mm). To sum up, the process parameters influence the melt pools, which in turn were found to affect the spinodal decomposition. Also, there is no presence of precipitates but elemental segregation indicating most probably the γ' precipitation would occur through spinodal decomposition instead of classical nucleation. In addition, it is quite clear that the increasing crack density with high energy input (*LED*) is not due to strain age cracking but solely due to solidification cracking.

Proxigrams generated with respect to Cr (9.5 at.%) iso-concentration surfaces are shown in Fig. 9. The proxigrams were generated from the whole run unlike the RDFs, which were performed on 30 nm cubes. A general trend observed from the proxigrams is that γ' forming elements such as Al, Ta and Ti tend to cluster together in the Al-rich regions and elements such as Cr, Co, and Mo cluster together in the Cr-rich regions. Also, there are other elements such as W, Si and B that do not show preferential segregation. Hf and C were found to cluster in the Al-rich regions but in a different manner. The concentrations of Hf and C were found to be higher for the sample processed with *LED* of 0.1 J/mm (Fig. 9**(g)**) than the samples with *LED* of 0.2 J/mm (Fig. 9**(h)**) and 0.3 J/mm (Fig. 9**(i)**). It is possible that this can be caused by the different process parameters and the stronger laser overlap (remelting). However, this would require further investigation and perhaps site-specific lift outs and multiple samples to come to a definite conclusion. On this regards it is important to point out that the melt pool size ranges in the hundreds of microns, while the APT reconstructions are in the hundreds of nanometers. Any local inhomogeneity in chemical composition and elemental distribution over the scale of the melt pool size, could

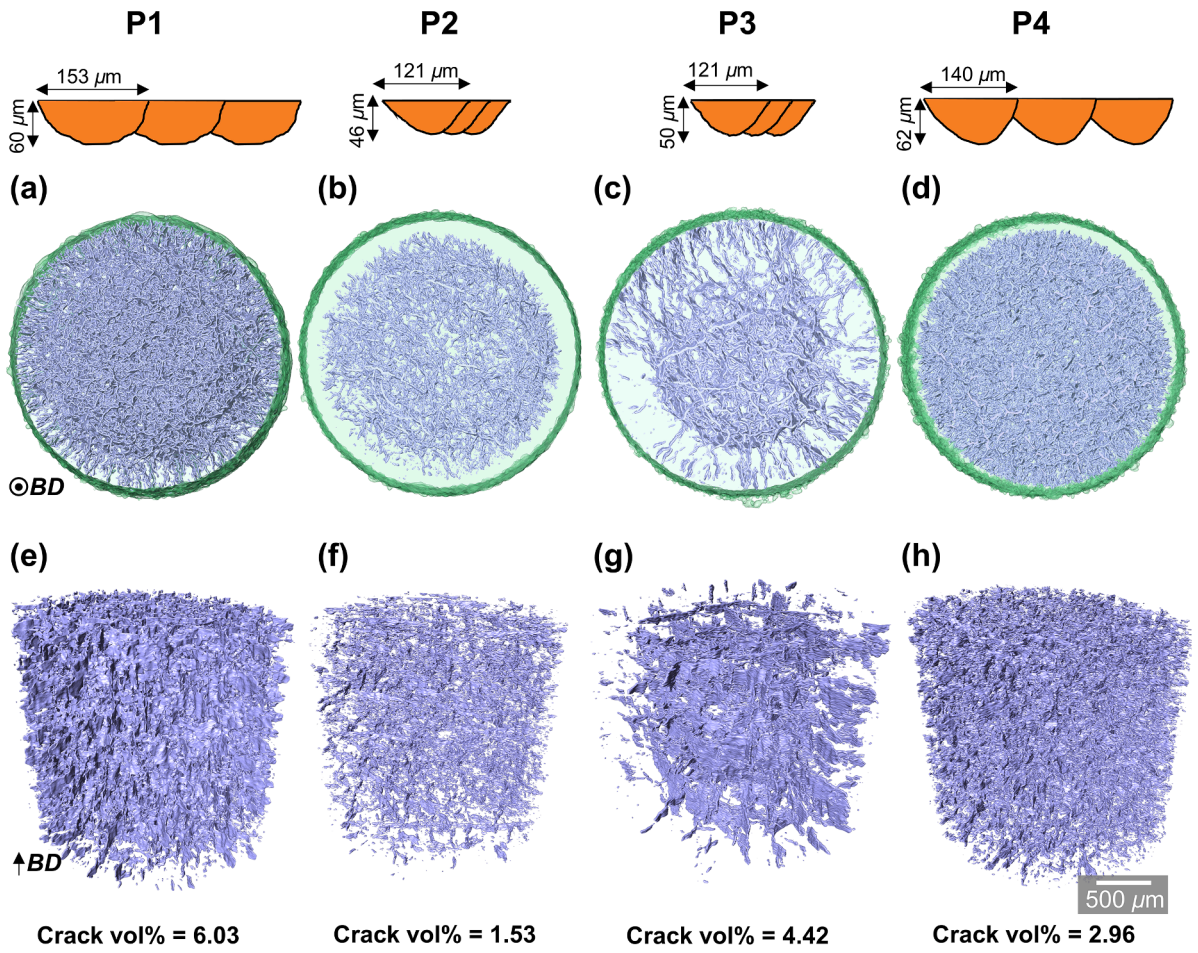

Fig. 7. X-ray computed tomography (CT) for different process parameters. **(a),(e)** P1 (74 J/mm^3): $P = 100$ W, $v = 500$ mm/s, $h = 0.09$ mm, **(b), (f)** P2 (74 J/mm^3): $P = 200$ W, $v = 3000$ mm/s, $h = 0.03$ mm, **(c), (g)** P3 (111 J/mm^3): $P = 300$ W, $v = 3000$ mm/s, $h = 0.03$ mm, **(d), (h)** P4 (53 J/mm^3): $P = 200$ W, $v = 1750$ mm/s, $h = 0.09$ mm.

potentially affect the APT results. To confirm that there were no inhomogeneities in the chemical composition SEM-EDS analysis was performed on a magnification of 500X over the entire area and the results are tabulated in Table 5. It was observed that there were no inhomogeneities and the composition obtained from EDS for the samples with different *LED* (0.1, 0.2 and 0.3 J/mm) were similar to the composition of the feedstock. The only exception was Hf which was lower than in the powder feedstock, but the composition of the bulk was similar, and we can assume there are no inhomogeneities on this scale. Hence, any differences observed in APT are likely due to inhomogeneities at the melt pool size.

4. Discussion

This study explored the PBF-LB processability of CM247LC. The effect of laser process parameters (power, speed, and hatch) on solidification cracking, melt pool geometry, microstructure and residual stress have been presented above. The results indicate that there is a correlation between the laser process parameters, melt pool geometry, grain morphology and texture, which ultimately affects the solidification cracking. Additionally, the study also demonstrated that segregation at the atomic level can possibly be influenced by the melt pool shape, which has not been described in the literature before.

4.1. Impact of process parameters on melt pool, microstructure and solidification cracking

The effect of laser process parameters such as power, speed, and hatch, did not have a significant effect on solidification cracking. However, it was seen that the combination of the process parameters like *LED,* which is the ratio of power and speed (*P/v*), had a major influence on the solidification cracking (measured as crack density). It was observed that samples with low *LED* ($\leq$ 0.1 J/mm) had low crack density compared to samples with high *LED* ($\geq$ 0.2 J/mm). The reason for this behavior is the extent of the mushy zone and the solidification structure. From the hot cracking criterion (RDG model) developed by Rappaz, Drezet and Gremeau [44], it is known that a large mushy zone is likely to cause solidification cracking. In order to investigate the effect of *LED* on the mushy zone, the Additive Manufacturing Module from Thermo-Calc 2024a was employed. The TCNI12 database was used for the Scheil solidification calculations. A steady-state calculation was used with a calibrated Gaussian heat source. The calibrated heat source had an absorptivity of 70 % and a beam diameter of ~80 μm. The keyhole model with a Rayleigh length of 2.5 mm was used. The top boundary condition had a radiation emissivity of 0.8 and a convective heat transfer coefficient of 20 W/m^2. Evaporation was also considered in the simulations.

Fig. 10**a** shows a simulation performed for a parameter set with equivalent *LED* of 0.3 J/mm. Isosurfaces are used to represent the solidus ($T_{Solidus}$) and the liquidus ($T_{Liquidus}$) temperatures. The $T_{Liquidus}$ isosurface appearing in red color is the region that is above the liquidus temperature, i.e. the melt pool. The $T_{Solidus}$ isosurface appearing in blue

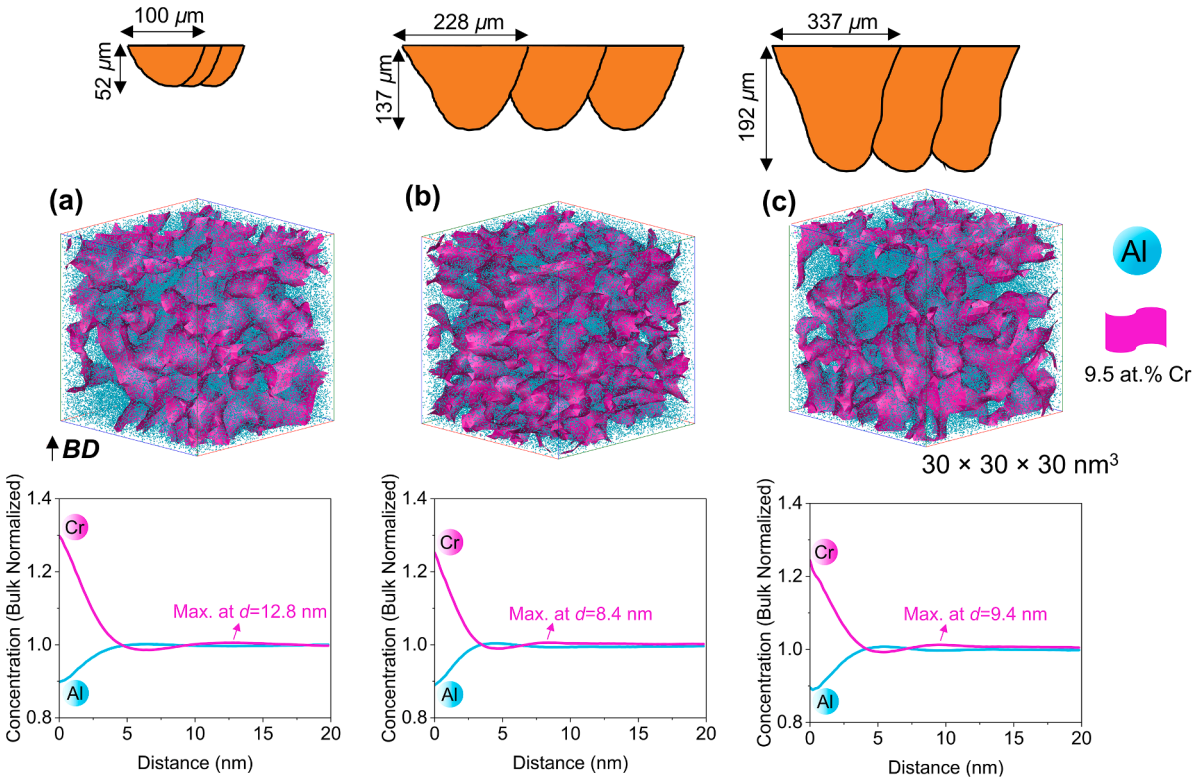

Fig. 8. APT of a cube of 30 nm with normalized radial distribution function (RDF) along with the melt pool geometries for the parameters used to build the sample. **(a)** *LED* (P/v) = 0.1 J/mm & h = 0.03 mm, **(b)** *LED* (P/v) = 0.2 J/mm & h = 0.06 mm, **(c)** *LED* (P/v) = 0.3 J/mm & h = 0.09 mm. The corresponding E* values for (a), (b) and (c) are 2.61, 5.22 and 8.70. Al atoms are indicated by points and Cr is indicated by iso-concentration surface of 9.5 at.%.

color is the region that has temperatures between $T_{Solidus}$ and $T_{Liquidus}$ and is referred to as the mushy zone. The lengths of the mushy zone (L_{mushy}) were then measured for different *LED* (0.1, 0.2 and 0.3 J/mm) and are shown in Fig. 10b along with the crack density. It is seen that for *LED* of 0.1 and 0.2 J/mm, the crack densities are similar (~2.19 and 2.16 mm/mm^2, respectively). For an *LED* of 0.2 J/mm, there is a higher crack density and the largest mushy zone length. The reason for the similar crack densities for *LED* of 0.1 and 0.2 J/mm despite the larger mushy zone for 0.2 J/mm can be attributed to the solidification structure. For both 0.1 and 0.2 J/mm, the solidified cellular structure is nearly parallel to the build direction (Fig. 10**c,d**). It can also be observed from Fig. 5**a, d** that they have columnar and highly textured microstructure. This shows that both the solidification structure and grain morphology can play a crucial role in minimizing solidification cracking. This can be explained by applying the concept of 'attractive' and 'repulsive' grain boundaries by Rappaz [45]. Based on this model, there is a possibility that high angle grain boundaries (HAGBs) are more prone to segregation and liquid film formation at lower temperatures. This difference would be the reason for higher crack susceptibility of HAGBs [18,45,46]. This can be observed in Fig. 10e, where a crack was formed when the solidifying cellular structures had higher misorientation and possibly a HAGB. Hence, it is suggested that although it is important to have a low *LED* (in order to have a smaller mushy zone), it is even more important to control the grain morphology and the texture if one wants to minimize solidification cracking in materials like CM247LC.

It was also demonstrated that the volumetric energy $VED = P/(v.h.t)$, where P = laser power, v = speed, h = hatch spacing and t = layer thickness), had no clear relation with solidification cracking. However, it was observed that for samples processed with low *LED* (~0.1 J/mm), it was crucial to have a small hatch spacing to have sufficiently high *VED*. The physical meaning behind the results mentioned above can be described by using the melt pool as a building block as shown in Fig. 11. First of all, it is important to have the right building block, i.e. a melt pool shape with low crack density. It was observed from Fig. 4 **(a, b)** that shallower and narrower melt pools obtained when processing with low *LED* have low crack density, as which has also been reported in welding literature [47]. So, after choosing the right building block (*LED* = 0.1 J/mm as shown in Fig. 11), one has to to choose the arrangement of the building blocks. Here it is important to choose the horizontal distance between the melt pools, i.e. hatch spacing. Since the melt pools are shallow and narrow, using typical hatch spacings (h_1) would not be optimal, as it will lead to lack of fusion defects. Therefore, using small hatch spacing h_2 eliminates the risk of lack of fusion (shown in Fig. 11).

Grange et al. [17] demonstrated that controlling the melt pool size and having a strong overlap ratio, i.e. a small hatch spacing, minimized solidification cracking in IN738LC. It was also concluded that the remelting occurring for a high overlap ratio caused crack healing. In this study on CM247LC it was found that the crack density decreased when hatch spacing was increased from 0.03 to 0.09 mm for samples processed with the lowest *LED* (Table 3). For samples with increased *LED*, however, the crack density increased, when the hatch spacing was increased (from 0.06 to 0.09 mm). This abnormal behavior can be explained by observing the grain morphology of these samples (see Fig. 5**)**. It is observed that there is a transition from long columnar to fine equiaxed grains with increasing hatch spacing for low *LED* (Fig. 5**(a–c)**). It is also observed from the pole figures that the texture becomes weaker (see Fig. 5**(a–c)**). This change in grain morphology and texture with increasing hatch spacing for a fixed *LED* is most probably the reason for the lower crack density. On the other hand, for increased *LED* and an intermediate hatch spacing we have a strong texture (Fig. 5**d**). Also, it is known that solidification cracking occurs in high angle grain boundaries (HAGBs), typically greater than 10 to 15° [46]. This type of HAGBs is less frequent for the sample in Fig. 5**d** than Fig. 5**e,** which explains why a lower crack density is observed for this sample in Fig. 1**d** than Fig. 1**e.** Similar observations have also been reported in the literature. In particular, Kumar et al. [11] reported that CM247LC samples processed

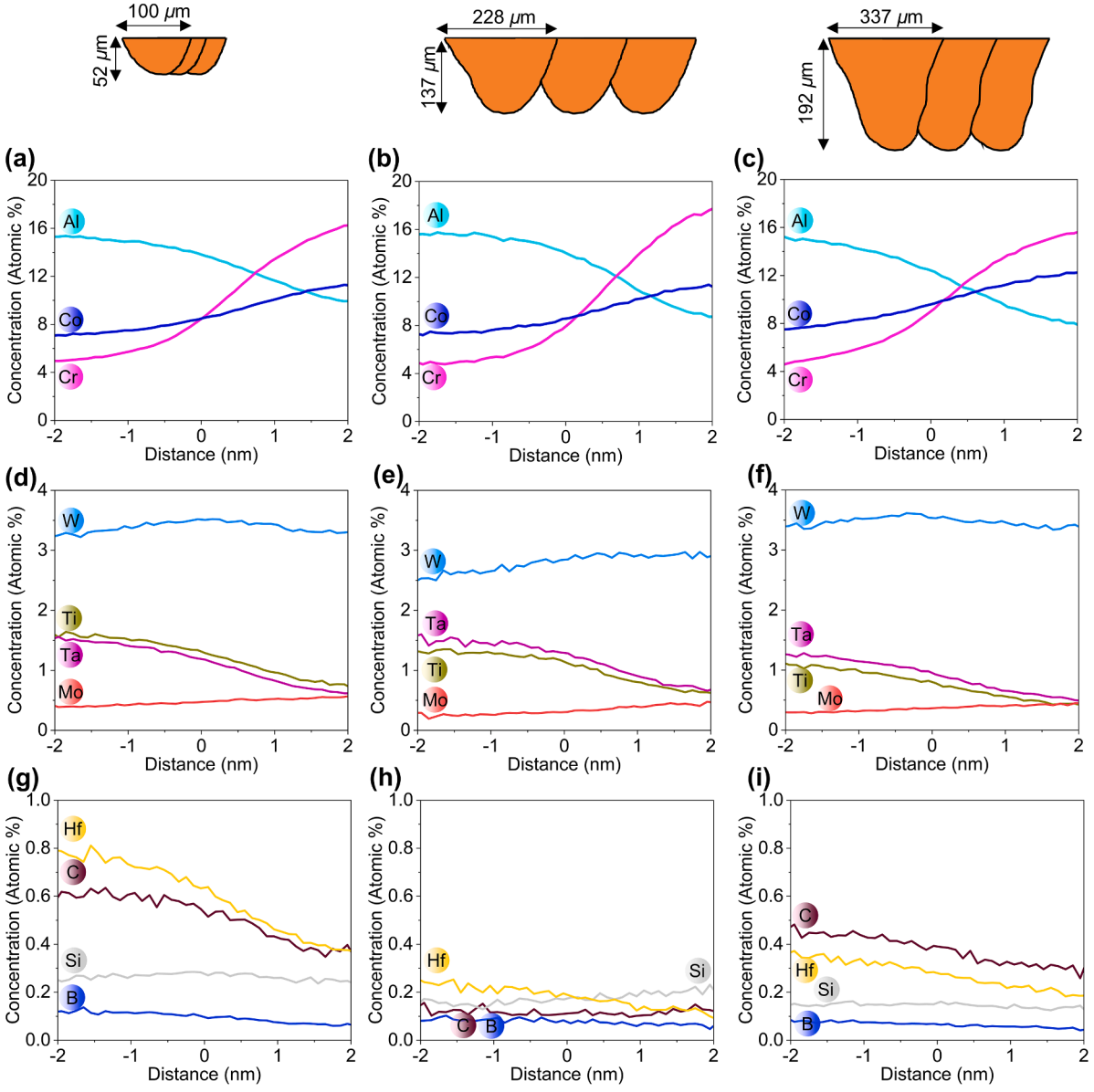

Fig. 9. Proxigrams obtained across 9.5 at.% Cr iso-concentration surface along with melt pool geometries. **(a), (d), (g)** processed with *LED* (P/v) = 0.1 J/mm & h = 0.03 mm. **(b), (e), (h)** processed with *LED* (P/v) = 0.2 J/mm & h = 0.06 mm. **(c), (f), (i)** processed with *LED* (P/v) = 0.3 J/mm & h = 0.09 mm.

Table 5
Composition of CM247LC powder feedstock and bulk samples (measured using EDS). (a) processed with *LED* (P/v) = 0.1 J/mm & h = 0.03 mm. (b) processed with *LED* (P/v) = 0.2 J/mm & h = 0.06 mm. (c) processed with *LED* (P/v) = 0.3 J/mm & h = 0.09 mm.

wt.%	Cr	Co	Mo	C	W	Hf	Ta	Ti	Al	Zr	B	Si	Ni
Powder	8	9.3	0.5	0.06	9.7	1.3	3.2	0.8	5.6	0.009	0.01	0.08	Bal.
(a)	8.26	9.44	0.68	–	9.91	0.56	3.69	0.73	5.62	0.18	–	–	Bal
(b)	8.27	9.47	0.60	–	10.52	0.46	4.08	0.73	5.41	0.00	–	–	Bal
(c)	8.25	9.28	0.48	–	10.76	0.57	3.66	0.78	5.26	0.09	–	–	Bal

with *LED* of 0.44 J/mm had a higher fraction of HAGBs as opposed to samples with *LED* of 0.27 J/mm.

4.2. Role of volumetric energy density (VED) on residual stresses

Residual stresses are stresses present in the part when there is no external loading applied. For PBF-LB, the differential shrinkage/expansion due to repeated melting and solidification along with phase transformations can lead to formation of stress between different phases or different positions in a part. On the other hand, the thermal tensile stress formed within a melt pool acting on the liquid film during the last stages of solidification leads to solidification cracking. One can consider that the residual stress measured in this study using XRD are on the *macro/meso* scale and permanent in nature, while the thermal stresses leading to solidification cracking are at the *micro* scale and transient. It can be argued that a component with increased solidification cracking could have residual stress relaxation. But in this study, it was found that the residual stress scales with the *VED*. Two samples with different

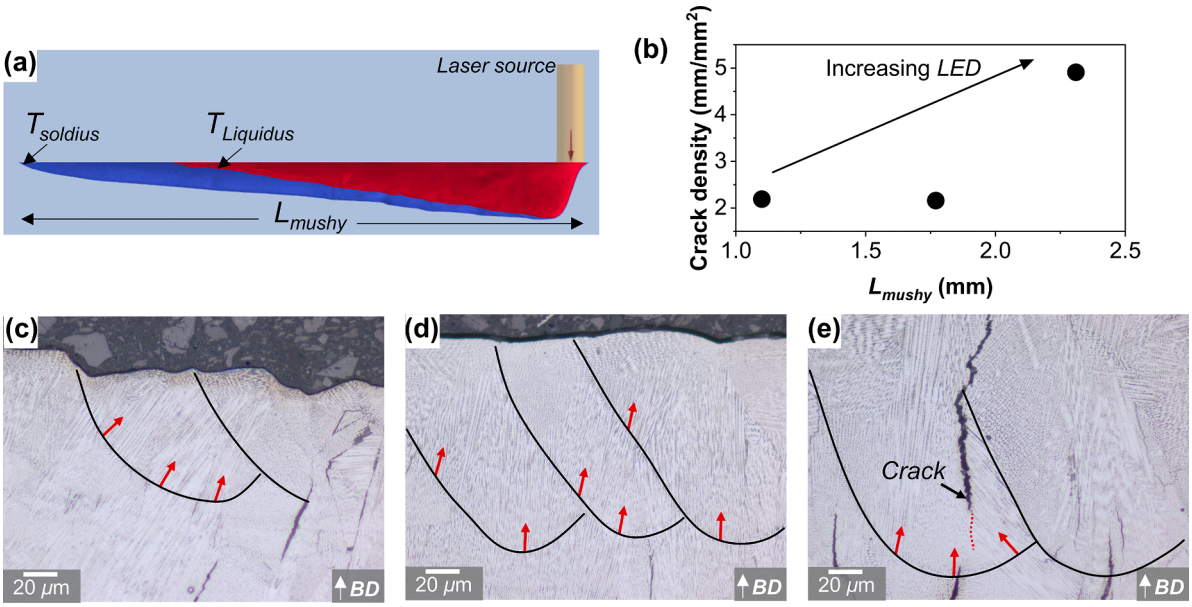

Fig. 10. (a) Simulation showing the melt pool + mushy zone for *LED* of 0.3 J/mm showing the length of the mushy zone (L_{mushy}) along with the solidus and liquidus temperatures used for the isosurfaces. (b) Correlation between the length of the mushy zone from the simulation and crack densities for different LEDs shown in (c)-(e). The simulation was done using the Additive Manufacturing Module in ThermoCalc 2024a. TCNI12 database was used for calculating the Scheil solidification curve. (c)-(e) LOM etched micrographs showing melt pools for samples processed with LED of (c) 0.1 J/mm, (d) 0.2 J/mm and (e) 0.3 J/mm.

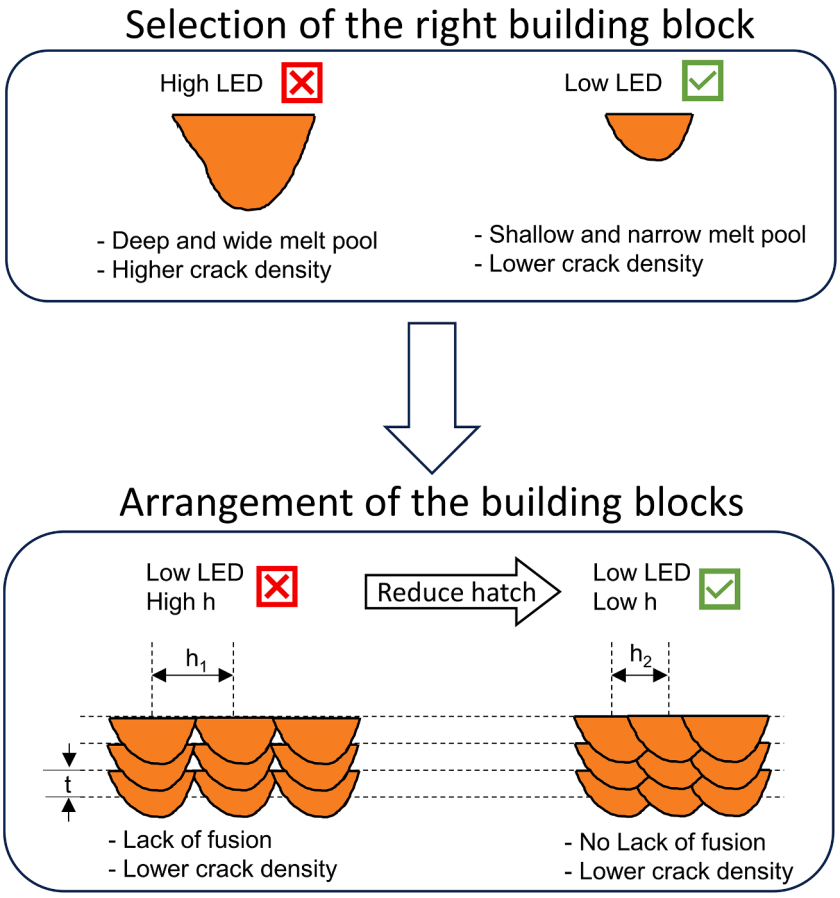

Fig. 11. Schematic showing the impact of melt pool geometry and arrangement on defect type and content as well as the proposed methodology for the selection of the right building block based on *LED* and their arrangement for defect-free processing of non-weldable alloys such as CM247LC.

process parameters but with the same *VED* had similar residual stress values. This signifies that *VED* had a more important effect than individual laser process parameters on residual stress buildup despite having different crack densities. It can also be noted (see Fig. 6 and Table 4) that the residual stress seems not to be influenced by the *LED* or the melt pool geometry. A possible explanation for the strong effect of *VED* on residual stress is the thermal gradient within the part. It is likely that a higher *VED* can lead to larger thermal gradients, and, in turn, higher residual stresses. Another future study to be considered is to process with the same *VED* (same process parameters) but with different crack densities to study the impact of the extent of solidification cracking on residual stresses. This is because it is challenging to deconvolute the extent of stress relaxation occurring due to solidification cracking. A possible way of achieving this is by modifying the alloy composition to increase solidification cracking. This could reveal the relation between solidification cracking and residual stresses in a controlled experiment.

The reported residual stress values at larger depths (Fig. 6) are equal to or greater than the room temperature yield strength of as-built CM247LC (~800 to 900 MPa) [48]. From the von Mises yielding criterion for multiaxial loading, it can be inferred that a triaxial tensile stress state likely existed, allowing a stress greater than the yield strength for uniaxial loading to be retained in the building direction. Although the stress component normal to the face could not be assessed using the $\sin^2\psi$ method, a tensile stress of between 100 and 200 MPa was indeed found in the transverse direction. Further, it can be noted that the $\sin^2\psi$ method was derived based on the assumption of isotropic elastic behavior in the probed volume. Such an assumption probably would not be the case for the current samples. Obvious diffraction peak intensity oscillations with ψ angles were observed from at depths larger than 100 μm especially for P1 to P3, revealing the presence of texture. Thus, measurement errors might have risen due to anisotropic elasticity related to the texture and contributed to the high residual stress values. Nevertheless, it is known that residual stresses must be balanced, and the tensile surface residual stresses are balanced by compressive residual stresses in the bulk [40]. Also, the chosen diffraction elastic constants (DECs) influence the resulting stress values [49]. They can be different for conventionally manufactured materials compared to PBF-LB. Due to the lack of information in the literature about DEC for PBF-LB CM247LC, the value for cast CM247LC was used. This choice does not affect the comparison between the samples, and comparative values must be borne in mind, rather than absolute values.

An additional finding was that low residual stress values were obtained for samples processed with low *VED*. This can be due to the lower energy input to the material leading to small thermal gradients and in turn low residual stresses. Another hypothesis is that the presence of lack of fusion defects aids residual stress relaxation. Although it is crucial to lower the residual stresses, processing CM247LC with low *VED* would lead to more lack of fusion defects (see Fig. 6**d**), which can be difficult to close during post-processing steps such as HIP. On the other hand, samples processed with a high *VED* can have cracks with plate-like morphology open to the surface that cannot be closed by HIP. So, it is recommended to have moderate *VED*, in order to minimize the crack density and amount of lack of fusion defects, which can be healed by HIP. Other strategies such as preheating, modified scan strategies or tailored post heat treatments should be explored for minimizing the residual stress further to reduce the strain age cracking risk [50–52].

4.3. Spinodal decomposition and absence of γ' precipitation

Segregation at the nanoscale, studied by APT, was found to be related to the melt pool size (Figs. 8 and 9). The spinodal decomposition of mainly Cr and Al was found in the as-built microstructure, and such clustering was also shown for high γ' Ni-base superalloys through APT in the literature [43,53]. However, similarly to the results reported in this work, none of the studies showed presence of γ' precipitates in the as-built condition. This is an indication that the high cooling rates (~10^6 to 10^7 K/s) in PBF-LB probably suppresses the formation of γ' [1,54,55]. However, it is suspected that spinodal decomposition could play a role in the early stages of γ' nucleation [56]. Studying the γ' precipitation kinetics was beyond the scope of this study, but findings by Collins et al. [56] showed that similar fluctuations in concentration were observed in the APT of the Ni-base superalloy (RR1000) gas atomized powder (cooling rate of 10^4 to 10^6 K/s [55,57]). In no case the spinodal decomposition is reported to have developed to the late stages where different phases can be found.

Certain studies, however, have indicated the presence of γ' precipitates in as-built condition [23,58,59]. Després and co-workers [23] found γ' precipitates located along the grain boundaries using APT in a superalloy with Al and Ti content of about 2.3 wt% and 3.1 wt.%, respectively. Similarly Divya et al. [58] found that γ' precipitates with a binomial distribution were found in the cell boundaries in as-built CM247LC using transmission electron microscopy (TEM). Both studies have found precipitates at boundaries (cellular/grain), where there can be differences in segregation due to the complex thermal history of the PBF-LB process. This could have ultimately led to precipitation of γ' at the boundaries. On the other hand, Miller and co-workers [59] found that IN713LC (similar Al and Ti content as CM247LC) also had γ' precipitates in as-built condition using TEM. However, the presence of γ' was not evident from APT reconstructions. Furthermore, a recent finding from Schulz et al. [53] was that there were no γ' precipitates found in as-built condition using either TEM or APT for IN738LC. Supposedly, there can be differences in the processing conditions employed that can lead to differences in γ' precipitation in as-built condition. Also, the alloying elements can possibly have some effect. For example, IN713LC does not contain high quantities of refractory elements, unlike CM247LC (W+Hf+Ta > 14 wt.%). Refractory elements are slowly diffusing elements that affect the γ' precipitation kinetics. To sum up, one can say that the presence of γ' precipitates can be heavily dependent on the alloy chemistry, processing conditions, site of investigation and the characterization technique. For the parameters employed within this study and for CM247LC, no γ' formation was observed using APT in the bulk and it is safe to assume that strain age cracking has not been observed in the as-built state.

The separation of the elements towards Cr-rich or Al-rich regions observed in Fig. 9 can be attributed to the partitioning coefficients (k) of each element. The partitioning coefficient is defined as the ratio of the atomic fraction of the element in the γ' and γ phase, respectively. Elements like Cr, Co, Mo and W with $k < 1$ tend to partition together and these are the elements which tend to be enriched in the γ phase. On the other hand, elements like Al, Ti, Hf and Ta with $k > 1$ tend to be enriched in the γ' phase. This reaffirms the previously established point that there will be further elemental partitioning during heat treatment, and spinodal decomposition will promote the concentration of γ'-formers in the Al-rich regions. This can in turn promote γ' precipitation. Another observation was that there were differences in the Cr and Al segregation from the RDF in Fig. 8 where the extent of spinodal decomposition was affected by the deposition parameters. The sample with *LED* of 0.1 J/mm had longer spinodal wavelength than the samples with *LED* of 0.2 J/mm and 0.3 J/mm. This means that the sample with *LED* of 0.1 J/mm had decomposed to a greater extent, possibly due to the higher degree of remelting linked to the tight hatch spacing that characterizes this sample. There is no concrete evidence that would allow to correlate spinodal decomposition and solidification cracking in Ni-base superalloys. However, spinodal decomposition in heat-treated high Cr content steels is known to play a role in increasing hardness and decreasing ductility. Verifying this link for Ni-base superalloys would require more extensive APT work coupled with mechanical testing and could be a topic for future research.

5. Conclusions

This study investigated the relationship between PBF-LB process

parameters, defect formation, melt pool geometry, grain morphology, residual stresses, and segregation for the non-weldable Ni-base superalloy CM247LC. The following are the main conclusions that can be drawn from the study:

- The cracking observed in as-built CM247LC was most probably due to solidification cracking. The absence of γ' precipitates from APT confirms that the cracking is not due to strain age cracking.
- Processing with low *LED* leads to shallow and narrow melt pools with less solidification cracking. This also means that the hatch spacing shall be small to avoid lack of fusion, i.e. a sufficiently high *VED* is needed.
- The solidification cracking was also found to be affected by grain morphology and texture. Samples with small grains were found to have less solidification cracking. Another observation was that minimizing the fraction of HAGBs could also minimize solidification cracking.
- It is not possible to completely eliminate cracking in CM247LC. Further optimizations such as modified scanning strategies, tailoring the composition or increased pre-heating would have to be explored.
- The residual stresses were affected primarily by the *VED*. Residual stresses were proportional to the *VED* used to process the material. Also, samples processed with the same *VED*, but with different process parameters, had similar residual stresses. It is of interest to minimize the residual stress to minimize the risk of strain age cracking during post-process heat treatment. However, there needs to be a compromise as there is risk of lack of fusion at lower *VED*.
- APT indicated that there were no precipitates in the as-built condition, but elemental segregation indicating early stages of spinodal decomposition. The sample processed with low *LED* (0.1 J/mm) was found to be decomposed more than samples processed with higher *LED* (0.2 and 0.3 J/mm). This is attributed to the increased remelting/reheating and the complex thermal history.

Data availability

The data that supports the findings of this paper are available from the authors on reasonable request.

CRediT authorship contribution statement

Ahmed Fardan: Conceptualization, Investigation, Visualization, Writing – original draft. **Andrea Fazi:** Investigation, Visualization, Writing – review & editing. **Ru Lin Peng:** Investigation, Writing – review & editing. **Tatiana Mishurova:** Investigation, Visualization, Writing – review & editing. **Mattias Thuvander:** Writing – review & editing. **Giovanni Bruno:** Writing – review & editing. **Håkan Brodin:** Conceptualization, Supervision, Writing – review & editing. **Eduard Hryha:** Conceptualization, Supervision, Writing – review & editing, Funding acquisition.

Declaration of competing interest

The authors declare that they have no known competing financial interests or personal relationships that could have appeared to influence the work reported in this paper.

Acknowledgements

This work has been performed in the framework of MAGDA (Materials for green hydrogen fueled gas turbines through additive manufacturing) project and the Centre for Additive Manufacturing – Metal (CAM^2), both supported by Swedish Governmental Agency for Innovation Systems (Vinnova). The APT investigations were carried out Chalmers Material Analysis Laboratory (CMAL) at Chalmers University of Technology.

Supplementary materials

Supplementary material associated with this article can be found, in the online version, at doi:10.1016/j.mtla.2024.102059.

References

[1] W.E. Frazier, Metal additive manufacturing: a review, J. Mater. Eng. Perform. 23 (2014) 1917–1928, https://doi.org/10.1007/s11665-014-0958-z.
[2] S. Sanchez, P. Smith, Z. Xu, G. Gaspard, C.J. Hyde, W.W. Wits, I.A. Ashcroft, H. Chen, A.T. Clare, Powder bed fusion of nickel-based superalloys: a review, Int. J. Mach. Tools Manuf. 165 (2021) 103729, https://doi.org/10.1016/j.ijmachtools.2021.103729.
[3] S.S. Babu, N. Raghavan, J. Raplee, S.J. Foster, C. Frederick, M. Haines, R. Dinwiddie, M.K. Kirka, A. Plotkowski, Y. Lee, R.R. Dehoff, Additive manufacturing of nickel superalloys: opportunities for innovation and challenges related to qualification, Metall. Mater. Trans. A Phys. Metall. Mater. Sci. 49 (2018) 3764–3780, https://doi.org/10.1007/s11661-018-4702-4.
[4] O. Adegoke, J. Andersson, H. Brodin, R. Pederson, Review of laser powder bed fusion of gamma-prime-strengthened nickel-based superalloys, Metals (Basel) 10 (2020) 1–26, https://doi.org/10.3390/met10080996.
[5] C. Guo, G. Li, S. Li, X. Hu, H. Lu, X. Li, Z. Xu, Y. Chen, Q. Li, J. Lu, Q. Zhu, Additive manufacturing of Ni-based superalloys: residual stress, mechanisms of crack formation and strategies for crack inhibition, Nano Mater. Sci. 5 (2023) 53–77, https://doi.org/10.1016/j.nanoms.2022.08.001.
[6] M. Lindbäck, K. Frankolin, E. Tuneskog, B. Karlsson, L. Wang, Development and validation under engine operation environment of addtively manufactured hot turbine parts, 2023. https://doi.org/10.1115/GT2023-103771.
[7] J.N. DuPont, J.C. Lippold, S.D. Kiser, Welding Metallurgy and Weldability of Nickel-Base Alloys, Wiley Online Library, 2009, https://doi.org/10.1002/9780470500262.
[8] J. Xu, P. Kontis, R.L. Peng, J. Moverare, Modelling of additive manufacturability of nickel-based superalloys for laser powder bed fusion, Acta Mater. 240 (2022) 118307, https://doi.org/10.1016/j.actamat.2022.118307.
[9] J.F.S. Markanday, K.A. Christofidou, J.R. Miller, E.R. Livera, N.G. Jones, E. J. Pickering, W. Li, Y. Pardhi, C.N. Jones, H.J. Stone, The microstructural evolution of CM247LC manufactured through laser powder bed fusion, Metall. Mater. Trans. A Phys. Metall. Mater. Sci. (2023), https://doi.org/10.1007/s11661-022-06939-0.
[10] S. Griffiths, H. Ghasemi Tabasi, T. Ivas, X. Maeder, A. De Luca, K. Zweiacker, R. Wróbel, J. Jhabvala, R.E. Logé, C. Leinenbach, Combining alloy and process modification for micro-crack mitigation in an additively manufactured Ni-base superalloy, Addit. Manuf. (2020) 36, https://doi.org/10.1016/j.addma.2020.101443.
[11] B. Kumar, S. Sahu, D. Srinivasan, N.J. Balila, Influence of heat input on solidification cracking in additively manufactured CM247LC Ni-based superalloy, Metall. Mater. Trans. A (2022), https://doi.org/10.1007/s11661-023-07027-7.
[12] Y.T. Tang, C. Panwisawas, J.N. Ghoussoub, Y. Gong, J.W.G. Clark, A.A.N. Németh, D.G. McCartney, R.C. Reed, Alloys-by-design: application to new superalloys for additive manufacturing, Acta Mater. 202 (2021) 417–436, https://doi.org/10.1016/j.actamat.2020.09.023.
[13] J.N. Ghoussoub, Y.T. Tang, C. Panwisawas, A. Németh, R.C. Reed, On the Influence of Alloy Chemistry and Processing Conditions On Additive Manufacturability of Ni-Based Superalloys, Springer International Publishing, 2020, https://doi.org/10.1007/978-3-030-51834-9_15.
[14] J.H. Boswell, D. Clark, W. Li, M.M. Attallah, Cracking during thermal post-processing of laser powder bed fabricated CM247LC Ni-superalloy, Mater. Des. 174 (2019) 107793, https://doi.org/10.1016/j.matdes.2019.107793.
[15] H. Hilal, R. Lancaster, D. Stapleton, G. Baxter, Investigating the influence of process parameters on the structural integrity of an additively manufactured nickel-based superalloy, Metals (Basel) 9 (2019), https://doi.org/10.3390/met9111191.
[16] R. Engeli, T. Etter, S. Hövel, K. Wegener, Processability of different IN738LC powder batches by selective laser melting, J. Mater. Process. Technol. 229 (2016) 484–491, https://doi.org/10.1016/j.jmatprotec.2015.09.046.
[17] D. Grange, J.D. Bartout, B. Macquaire, C. Colin, Processing a non-weldable nickel-base superalloy by selective laser melting: role of the shape and size of the melt pools on solidification cracking, Materialia 12 (2020), https://doi.org/10.1016/j.mtla.2020.100686.
[18] H. Gruber, E. Hryha, K. Lindgren, Y. Cao, M. Rashidi, L. Nyborg, The effect of boron and zirconium on the microcracking susceptibility of IN-738LC derivatives in laser powder bed fusion, Appl. Surf. Sci. 573 (2021) 151541, https://doi.org/10.1016/j.apsusc.2021.151541.
[19] L.N. Carter, M.M. Attallah, R.C. Reed, Laser powder bed fabrication of nickel-base superalloys: influence of parameters; characterisation, quantification and mitigation of cracking, in: Proc. Int. Symp. Superalloys, 2012, pp. 577–586, https://doi.org/10.7449/2012/superalloys_2012_577_586.
[20] O. Adegoke, J. Andersson, H. Brodin, R. Pederson, Influence of laser powder bed fusion process parameters on voids, cracks, and microhardness of nickel-based superalloy alloy 247LC, Materials (Basel) 13 (2020) 1–23, https://doi.org/10.3390/MA13173770.
[21] J.N. Ghoussoub, Y.T. Tang, W.J.B. Dick-Cleland, A.A.N. Németh, Y. Gong, D. G. McCartney, A.C.F. Cocks, R.C. Reed, On the influence of alloy composition on the additive manufacturability of Ni-based superalloys, Metall. Mater. Trans. A 53 (2022) 962–983, https://doi.org/10.1007/s11661-021-06568-z.

[22] H.Y. Wang, Y.L. Lo, H.C. Tran, M.M. Raza, T.N. Le, Systematic approach for reducing micro-crack formation in Inconel 713LC components fabricated by laser powder bed fusion, Rapid Prototyp. J. 27 (2021) 1548–1561, https://doi.org/10.1108/RPJ-11-2020-0282.
[23] A. Després, S. Antonov, C. Mayer, C. Tassin, M. Veron, J.J. Blandin, P. Kontis, G. Martin, On the role of boron, carbon and zirconium on hot cracking and creep resistance of an additively manufactured polycrystalline superalloy, Materialia 19 (2021), https://doi.org/10.1016/j.mtla.2021.101193.
[24] H.E. Huang, C.H. Koo, Effect of zirconium on microstructure and mechanical properties of cast fine-grain CM 247 LC superalloy, Mater. Trans. 45 (2004) 554–561, https://doi.org/10.2320/matertrans.45.554.
[25] D.K. Ganji, G. Rajyalakshmi, Influence of alloying compositions on the properties of nickel-based superalloys: a Review, in: Lect. Notes Mech. Eng., 2020, pp. 537–555, https://doi.org/10.1007/978-981-15-1071-7_44.
[26] J. Xu, High-Performance Nickel-based Superalloys for Additive Manufacturing, Linköping University, 2022, https://doi.org/10.3384/9789179292584.
[27] J. Xu, H. Gruber, R.L. Peng, J. Moverare, A novel γ′-strengthened nickel-based superalloy for laser powder bed fusion, Materials (Basel) 13 (2020) 1–12, https://doi.org/10.3390/ma13214930.
[28] A. Jena, S.E. Atabay, A. Gontcharov, P. Lowden, M. Brochu, Laser powder bed fusion of a new high gamma prime Ni-based superalloy with improved weldability, Mater. Des. 208 (2021) 109895, https://doi.org/10.1016/j.matdes.2021.109895.
[29] A.B. Gontcharov, P. Lowden, A. Jena, S. Kwon, M. Brochu, Weldability and properties of newly developed LW4280 high gamma prime nickel based superalloy for 3D am and repair of turbine engine components, Proc. ASME Turbo Expo 7 (2021) 1–10, https://doi.org/10.1115/GT2021-58851.
[30] L. Liu, D. Wang, G. Deng, Z. Liu, C. Tan, X. Zhou, C. Han, R. Jiang, Y. Yang, Crack inhibition to enhance strength-ductility of CM247LC alloy fabricated by laser powder bed fusion, Mater. Sci. Eng. A 875 (2023) 145114, https://doi.org/10.1016/j.msea.2023.145114.
[31] M. Gerstgrasser, M. Cloots, J. Stirnimann, K. Wegener, Focus shift analysis, to manufacture dense and crack-free SLM-processed CM247LC samples, J. Mater. Process. Technol. 289 (2021) 116948, https://doi.org/10.1016/j.jmatprotec.2020.116948.
[32] L.N. Carter, X. Wang, N. Read, R. Khan, M. Aristizabal, K. Essa, M.M. Attallah, Process optimisation of selective laser melting using energy density model for nickel based superalloys, Mater. Sci. Technol. (United Kingdom) 32 (2016) 657–661, https://doi.org/10.1179/1743284715Y.0000000108.
[33] M. Thomas, G.J. Baxter, I. Todd, Normalised model-based processing diagrams for additive layer manufacture of engineering alloys, Acta Mater. 108 (2016) 26–35, https://doi.org/10.1016/j.actamat.2016.02.025.
[34] J.C. Ion, H.R. Shercliff, M.F. Ashby, Diagrams for laser materials processing, Acta Metall. Mater. 40 (1992) 1539–1551, https://doi.org/10.1016/0956-7151(92)90097-X.
[35] K. Mukai, Z. Li, L. Fang, Measurement of the densities of nickel-based ternary, quaternary and commercial alloys, Mater. Trans. 45 (2004) 2987–2993, https://doi.org/10.2320/matertrans.45.2987.
[36] L. Avala, M. Bheema, P.K. Singh, R.K. Rai, S. Srivastava, Measurement of thermo physical properties of nickel based superalloys, Int. J. Mech. Eng. Robot. 1 (2013) 108–112.
[37] I.C. Noyan, J.B. Cohen, Residual Stress: Measurement by Diffraction and Interpretation, Springer, New York, NY, 1987, https://doi.org/10.1007/978-1-4613-9570-6.
[38] S. Ma, P. Rangaswamy, B.S. Majumdar, Microstress evolution during in situ loading of a superalloy containing high volume fraction of γ′ phase, Scr. Mater. 48 (2003) 525–530, https://doi.org/10.1016/S1359-6462(02)00504-3.
[39] Object Research Systems, Dragonfly 2020.2, (2023). http://www.theobjects.com/dragonfly.
[40] P. Pant, F. Salvemini, S. Proper, V. Luzin, K. Simonsson, S. Sjöström, S. Hosseini, R. Lin Peng, J. Moverare, A study of the influence of novel scan strategies on residual stress and microstructure of L-shaped LPBF IN718 samples, Mater. Des. 214 (2022) 110386, https://doi.org/10.1016/j.matdes.2022.110386.
[41] J. Schröder, A. Evans, V. Luzin, G. Abreu Faria, S. Degener, E. Polatidis, J. Čapek, A. Kromm, G. Dovzhenko, G. Bruno, J. Keckes, Texture-based residual stress analysis of laser powder bed fused Inconel 718 parts, J. Appl. Crystallogr. 56 (2023) 1076–1090, https://doi.org/10.1107/S1600576723004855.
[42] J. Zhou, J. Odqvist, M. Thuvander, P. Hedström, Quantitative evaluation of spinodal decomposition in Fe-Cr by atom probe tomography and radial distribution function analysis, Microsc. Microanal. 19 (2013) 665–675, https://doi.org/10.1017/S1431927613000470.
[43] O. Adegoke, C. Kumara, M. Thuvander, F. Deirmina, J. Andersson, H. Brodin, P. Harlin, R. Pederson, Scanning electron microscopy and atom probe tomography characterization of laser powder bed fusion precipitation strengthening nickel-based superalloy, Micron 171 (2023) 103472, https://doi.org/10.1016/j.micron.2023.103472.
[44] M. Rappaz, J.M. Drezet, M. Gremaud, A new hot-tearing criterion, Metall. Mater. Trans. A Phys. Metall. Mater. Sci. 30 (1999) 449–455, https://doi.org/10.1007/s11661-999-0334-z.
[45] M. Rappaz, A. Jacot, W.J. Boettinger, Last-stage solidification of alloys: theoretical model of dendrite-arm and grain coalescence, Metall. Mater. Trans. A Phys. Metall. Mater. Sci. 34A (2003) 467–479, https://doi.org/10.1007/s11661-003-0083-3.
[46] E. Chauvet, P. Kontis, E.A. Jägle, B. Gault, D. Raabe, C. Tassin, J.J. Blandin, R. Dendievel, B. Vayre, S. Abed, G. Martin, Hot cracking mechanism affecting a non-weldable Ni-based superalloy produced by selective electron Beam Melting, Acta Mater. 142 (2018) 82–94, https://doi.org/10.1016/j.actamat.2017.09.047.
[47] S. Kou, Weld metal solidification cracking, in: Weld Metallurgy, 2002, pp. 263–300, https://doi.org/10.1002/0471434027.ch11.
[48] X. Wang, L.N. Carter, B. Pang, M.M. Attallah, M.H. Loretto, Microstructure and yield strength of SLM-fabricated CM247LC Ni-superalloy, Acta Mater. 128 (2017) 87–95, https://doi.org/10.1016/j.actamat.2017.02.007.
[49] J. Schröder, A. Evans, T. Mishurova, A. Ulbricht, M. Sprengel, I. Serrano-Munoz, T. Fritsch, A. Kromm, T. Kannengießer, G. Bruno, Diffraction-based residual stress characterization in laser additive manufacturing of metals, Metals (Basel) 11 (2021), https://doi.org/10.3390/met11111830.
[50] V.P. Kumar, A.V. Jebaraj, Comprehensive review on residual stress control strategies in laser-based powder bed fusion process–Challenges and opportunities, Lasers Manuf. Mater. Process. 10 (2023) 400–442, https://doi.org/10.1007/s40516-023-00217-6.
[51] S. Chen, H. Gao, Y. Zhang, Q. Wu, Z. Gao, X. Zhou, Review on residual stresses in metal additive manufacturing: formation mechanisms, parameter dependencies, prediction and control approaches, J. Mater. Res. Technol. 17 (2022) 2950–2974, https://doi.org/10.1016/j.jmrt.2022.02.054.
[52] N. Bastola, M.P. Jahan, N. Rangasamy, C.S. Rakurty, A review of the residual stress generation in metal additive manufacturing: analysis of cause, measurement, effects, and prevention, Micromachines (2023) 14, https://doi.org/10.3390/mi14071480.
[53] F. Schulz, K. Lindgren, J. Xu, E. Hryha, Gamma prime formation in nickel-based superalloy IN738LC manufactured by laser powder bed fusion, Mater. Today Commun. (2023) 107905, https://doi.org/10.1016/j.mtcomm.2023.107905.
[54] P.V. Cobbinah, R.A. Nzeukou, O.T. Onawale, W.R. Matizamhuka, Laser powder bed fusion of potential superalloys: a review, Metals (Basel) 11 (2021) 1–37, https://doi.org/10.3390/met11010058.
[55] C. Pauzon, A. Raza, E. Hryha, P. Forêt, Oxygen balance during laser powder bed fusion of Alloy 718, Mater. Des. 201 (2021), https://doi.org/10.1016/j.matdes.2021.109511.
[56] D.M. Collins, N. D'Souza, C. Panwisawas, C. Papadaki, G.D. West, A. Kostka, P. Kontis, Spinodal decomposition versus classical γ′ nucleation in a nickel-base superalloy powder: an in-situ neutron diffraction and atomic-scale analysis, Acta Mater. 200 (2020) 959–970, https://doi.org/10.1016/j.actamat.2020.09.055.
[57] P. Fang, Y. Xu, X. Li, Y. Chen, Influence of atomizing gas and cooling rate on solidification characterization of nickel-based superalloy powders, Xiyou Jinshu Cailiao Yu Gongcheng/Rare Met. Mater. Eng. 47 (2018) 423–430, https://doi.org/10.1016/s1875-5372(18)30082-1.
[58] V.D. Divya, R. Muñoz-Moreno, O.M.D.M. Messé, J.S. Barnard, S. Baker, T. Illston, H.J. Stone, Microstructure of selective laser melted CM247LC nickel-based superalloy and its evolution through heat treatment, Mater. Charact. 114 (2016) 62–74, https://doi.org/10.1016/j.matchar.2016.02.004.
[59] J.R. Miller, J.F.S. Markanday, S.M. Fairclough, G.J. Wise, C.M.F. Rae, L.R. Owen, D. Stapleton, N. D'Souza, P.A.J. Bagot, H.J. Stone, Gamma prime precipitation in as-deposited Ni-based superalloy IN713LC, Scr. Mater. 239 (2024) 115775, https://doi.org/10.1016/j.scriptamat.2023.115775.